Numerical analysis of hemodynamics in intracranial aneurysms

Proposing a third hemodynamic criterion for predicting rupture sites

Merel Toussaint

Technische Universiteit Delft

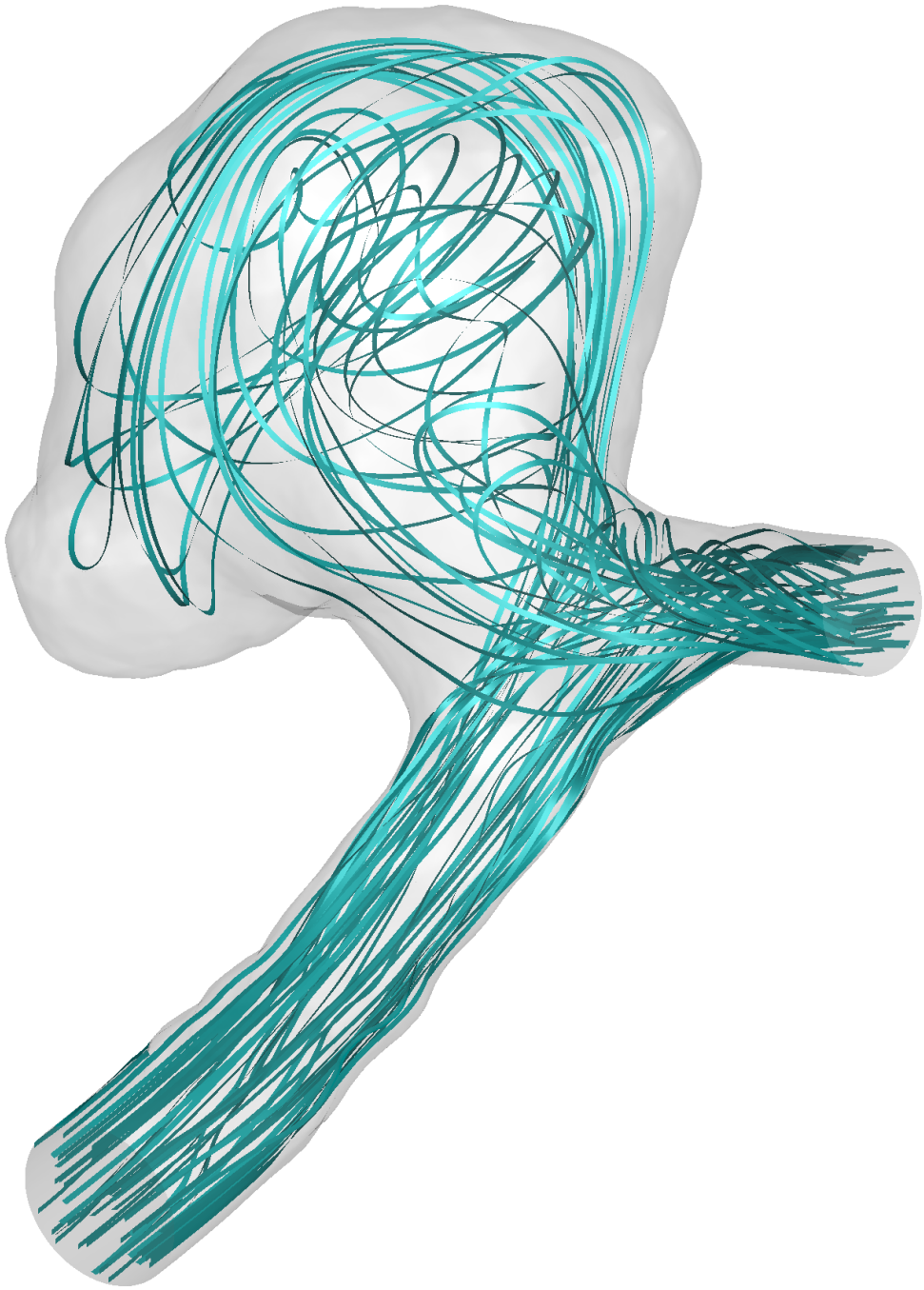

TU Delft Delft University of Technology

Challenge the future

Numerical analysis of hemodynamics in intracranial aneurysms

Proposing a third hemodynamic criterion for predicting rupture sites

by

Merel Toussaint

to obtain the degree of Master of Science

at the Delft University of Technology,

to be defended publicly on Wednesday May 23, 2018 at 10:00 AM.

Student number:	4095472	
Project duration:	August 22, 2017 – April 13, 2018	
Thesis committee:	Assoc. Prof. Dr. S. Kenjereš, Dipl.-Ing.,	TU Delft, supervisor
	Ir. R. Perinajová,	TU Delft
	Prof. Dr. C.R. Kleijn,	TU Delft
	Dr. N. Bhattacharya,	TU Delft
	Dr. P. van Ooij,	AMC Amsterdam

An electronic version of this thesis is available at http://repository.tudelft.nl/.

TU Delft

Abstract

Brain aneurysms cause almost 500,000 deaths in the world every year. A better understanding of brain aneurysm genesis and rupture may open new opportunities to prevention and treatment. In this study, a part of the cerebral vascular system, the so called circle of Willis including an aneurysm, was analyzed with Computational Fluid Dynamics (CFD). The importance of boundary conditions in an aneurysm simulation was assessed by comparing the results to 7T MRI velocity data, obtained from the Academic Medical Center (AMC) in Amsterdam. Adequate similarities were found in velocity values, together with qualitative agreement in wall shear stress (WSS) values.

We found that in a patient-specific case with an aneurysm, the velocity profile was able to develop to a parabolic profile because of its location; the aneurysm existed far downstream of the circle of Willis. This implies that it is possible to use a cropped arterial system to simulate the aneurysm and to use parabolic inlet velocity profiles for patients with this aneurysm phenotype.

In previous studies, it proved hard to locate the precise location of rupture in an aneurysm. A risk assessment of the rupture location in an aneurysm can be used as a more accurate tool to asses the need for surgery. The aneurysm geometry of the CFD Rupture challenge from 2013 (Janiga et al. [1] and Berg et al. [2], J of Biomech. Eng. 2015) was simulated to predict the location of a rupture site. This rupture location was predicted by combining the following hemodynamic criteria: the time-averaged wall shear stress (WSSTA), oscillatory shear index (OSI) and vortex-saddle point structure during systole with accompanying low pressure values. A sensitivity study was performed on these criteria and a critical threshold for rupture risk was proposed. Based on these criteria it was possible to predict the exact rupture site for two analyzed aneurysm geometries. It is concluded that a CFD model could be used to assess the hemodynamics in intracranial aneurysms. Future research should focus on repeating this study on more patient specific aneurysm geometries to verify this hypothesis further.

Preface

This thesis has been written as the final part of my master degree in Applied Physics at the Delft University of Technology. For about eight months I have been a guest in the Transport Phenomena group, where I had a desk next to my fellow students and was invited to be the student representative at the department meetings. The group was always very welcoming and I enjoyed coming to work there every day.

There are a few people I would like to thank for their support during this thesis project. First, Saša Kenjereš and Romana Perinajová for all positive and critical feedback on my work. They were always there to answer questions and have helped me to perform at my best. Then I would like to thank Pim van Ooij for showing and explaining the MRI data my research could be based on. He also invited me to give a presentation at the AMC, which was a nice opportunity to show my work.

Additionally, I thank the researchers from the Universität Magdeburg that organized the CFD Challenge and provided their geometry data for this study.

Natuurlijk wil ik ook graag nog even de mensen noemen die mij op andere vlakken hebben gesteund tijdens het schrijven van mijn thesis. Pap, mam, Ivo, Anne, David, Wiep, Lisanne, Jeffrey, Victor, Bart, Martine, Bas, Kiek en alle anderen: bedankt voor al jullie feedback, advies, koffie, knuffels en vooral tijd de afgelopen maanden!

Merel Toussaint
Delft, May 2018

Contents

Nomenclature

Acronyms

ACA	Anterior Cerebral Artery
ACoA	Anterior Communicating Artery
BA	Basilar Artery
CFD	Computational Fluid Dynamics
CoW	Circle of Willis
IA	Intracranial Aneurysm
ICA	Internal Carotid Artery
MCA	Middle Cerebral Artery
MRI	Magnetic Resonance Imaging
OSI	Oscillatory Shear Index
PCA	Posterior Cerebral Artery
SCA	Superior Cerebellar Artery
SIMPLE	Semi-Implicit Method for Pressure-Linked Equations
UDF	User Defined Function
VMTK	Vascular Modeling Toolkit
WSS	Wall Shear Stress
WSSTA	Wall Shear Stress time-average

Dimensionless Numbers

Re	Reynold's Number
St	Strouhal Number

Greek Symbols

$\dot{\gamma}$	Strain rate	s^{-1}
μ	Dynamic viscosity	$\mathrm{Pa\,s}$
ν	Kinematic viscosity	$\mathrm{m}^2\,\mathrm{s}^{-1}$
ω	Angular frequency of pulsating flow	$\mathrm{rad\,s}^{-1}$
ρ	Density	$\mathrm{kg\,m}^{-3}$

τ_w	Wall Shear Stress (WSS)	Pa

Roman Symbols

p	Pressure	Pa
Q	Volumetric flow rate	$\mathrm{m^3\,s^{-1}}$
R	Radius of a blood vessel	m
u	Velocity	$\mathrm{m\,s^{-1}}$

1

Introduction

Brain aneurysms cause almost 500,000 deaths in the world every year, which makes them an important topic of research [3]. Intracranial aneurysms are balloon-like expansions most frequently located in or around the Circle of Willis (CoW), which is a circle of arteries around the brain stem. Aneurysms do not necessarily give symptoms but are very dangerous when they grow or rupture. With the growth of the aneurysm, the pressure on the brain tissue increases, which might lead to headaches or loss of functions. A ruptured aneurysm causes a bleeding inside the subarachnoid space inside the head, which has a mortality rate of almost 50 % [4].

Currently, the precise cause of aneurysms is still unknown, but hypertension, atherosclerosis, abnormal flow at vessel junctions, heredity, and trauma are often mentioned as causes [5].

Aneurysms are often treated through surgery, when the aneurysm has ruptured or when the size exceeds a certain threshold [6], although research showed that size is not as important as the shape for rupture risk [7]. Another way of treatment is to fill the aneurysm sac with coils to prevent blood flow inside the aneurysm, so that the growth can be stopped. These procedures are not without risk for the patients. Therefore a non-invasive way to predict the growth of aneurysms could be a useful tool to calculate and assess these risks. Furthermore, the thresholds and guidelines present for the treatment of aneurysms are very general and developed with the use of statistics. Therefore it might be useful to find a way to assess the risk of rupture and the need for treatment on a patient by patient base. This thesis presents an assessment of CFD analyses as a tool to substantiate the rationale for treatment.

1.1. Previous research

MRI-CFD

Computational Fluid Dynamics (CFD) is a tool to model blood flow and oxygen transport in the human body. Magnetic Resonance Imaging (MRI) flow field measurements are used to provide boundary conditions for these simulations. These measurements often have a very low resolution, and the images are expensive and time consuming to make. Several studies have compared the results from CFD studies to 4D-MRI flow measurements in different arteries [8–13]. Some comparative CFD-MRI studies investigated intracranial aneurysms specifically [14–17]. Generally, the conclusion of these studies was that both methods agreed well.

Although CFD has a better resolution than the MRI results, MRI data is needed to provide proper boundary conditions and initial conditions for the simulations. Literature agrees on the fact that CFD and MRI complement each other.

Aneurysms

An objective of several CFD studies on intracranial aneurysms is to determine their cause or the location of their rupture. Absence or misshapes of parent arteries have an influence on the genesis of aneurysms [18], irregular Wall Shear Stress (WSS) values have an influence as well [19–21]. Furthermore, substances that influence the blood viscosity, like blood thinners or other medication, and therefore influence the WSS, are interesting to look at.

The flow patterns inside and surrounding several shapes of aneurysms have been investigated to elucidate the cause of their growth or even their rupture [22, 23]. However, very few examples are found of a CFD analysis of an entire CoW geometry including an aneurysm [24]. Next to that, more recent studies that did focus on the flow characteristics inside intracranial aneurysms, did not have access to any flow measurements. These studies used a generic heartbeat profile as initial conditions [25]. These studies do not assess the validity of these initial conditions.

Next to the evaluation of WSS values, another way to evaluate the risk of formation and rupture of aneurysms is the Oscillatory Shear Index (OSI) [26]. In literature, it is stated that the locations with a high OSI value and a low WSS are often used to find the locations with a high risk of rupture [1, 27–30]. As often multiple locations occur where the rupture risk is high, this set of criteria to find rupture sites is not complete. As described by Janiga et al. [1], Berg et al. [29] and Berg et al. [2], several research groups are able to predict several possible rupture sites inside an aneurysm, but most are not able to determine the actual rupture site. Furthermore, around half of the causes of aneurysm rupture cannot be found by evaluating hemodynamic properties, but are determined by the mechanical properties of the aneurysm wall [27]. Consequently, the combination between OSI and WSS as tool to predict possible rupture sites has limited clinical value. Is it possible to expand the criteria to better predict the rupture site location?

1.2. Goal of current research

This research builds on the work of Perinajová [13] by using her CFD model of a patient-specific CoW geometry. In this study, the workflow was optimized and the reproducibility of the previous CFD results was checked. After this phase, a more specific CFD research was performed on a CoW geometry with an intracranial aneurysm. This geometry was obtained from the Academic Medical Center in Amsterdam. The goal was to visualize the blood flow phenomena inside the intracranial aneurysm. So in this study a model was made of a geometry of the full CoW including an aneurysm. The first aim was to investigate the difference between naturally developed inflow boundary conditions in the aneurysm and forced-on boundary conditions at the inlet of the aneurysm. Secondly, simulations were performed on another aneurysm geometry, obtained from the CFD challenge in 2013 [1, 2], to investigate and expand the criteria to predict the rupture site. With a third criterion it was possible to predict the rupture location in the CFD challenge aneurysm, as well as for the AMC aneurysm.

The following research question was formulated: Can a CFD model be used to assess the hemodynamics in intracranial aneurysms and can this model predict the rupture site in an aneurysm? This research question is separated in a few sub-questions.

- To what extent is it possible to mimic MRI velocity measurement data with CFD simulations?
- What effect do blood thinners have on velocity profiles and WSS values inside the arteries of the CoW?
- What effect do inlet velocity profiles have on flow structure and WSS values in aneurysms?
- Which parameters next to the Oscillatory Shear Index (OSI) and Wall Shear Stress Time-Average (WSSTA) can be found as criteria for the risk of aneurysm rupture?

1.3. Outline

In Chapter 2, the background is presented, to provide a link between Transport Phenomena and Biology. The methods of simulation and underlying theories will be covered in Chapter 3. Initialization and results of the simulations regarding the healthy CoW geometry are given in Chapter 4. In Chapter 5 the results of all aneurysm models and the discussion of their implication will be covered. Chapter 6 will cover the results of the simulations from the CFD rupture challenge. Concluding remarks are given in Chapter 7 and finally, some recommendations will be made in Chapter 8.

2

Theoretical background

This section provides background in the fields this research touches upon. Information about biological systems as well as transport phenomena is given.

2.1. Biology

2.1.1. Circle of Willis

The Circle of Willis (CoW) is a ring of connected arteries surrounding the brain stem. The alleged purpose of this circle is that all parts of the brain can still be provided with oxygen if one of the supplying arteries is stenosed or blocked. The blood enters the CoW via the Basilar Artery (BA) on the posterior side and via the left and right Internal Carotid Arteries (ICA) on the anterior side. Six major arteries exit the CoW: The left and right Anterior Cerebral Arteries (ACA), which are connected by the Anterior Communicating Artery (ACoA), the left and right Middle Cerebral Arteries (MCA), and the left and right Posterior Cerebral Arteries (PCA). At the sides of the BA, the left and right Superior Cerebellar Arteries (SCA) are situated. The location of these arteries is visualized in Figure 2.1.

When parts of the CoW are underdeveloped, neighboring arteries may grow in size to take over their function, but these abnormalities often hinder the hemodynamic balance inside the arteries [31, p.556]. The consequences of underdeveloped or missing parts of the CoW have been studied intensively [13], [32]: the flow rate of the inflow arteries (BA and ICAs) is decreased as their downstream connected arteries are blocked or not present. The ability of blood vessels to adapt to certain circumstances is elaborated on in the next paragraph.

2.1.2. Blood vessels

Arterial walls in the human body consist of three layers, tunica intima, tunica media and the tunica adventitia. The tunica intima is the inner layer. It consists of a single cell layer called the endothelium and some elastic tissue that connects the endothelium to the tunica media. The tunica media is the thickest layer in the middle of the arterial wall and consists of smooth muscle fibers. This layer is able to change the diameter of the blood vessel to influence the flow rate through the artery. This muscle layer is surrounded by elastic connecting tissue. The

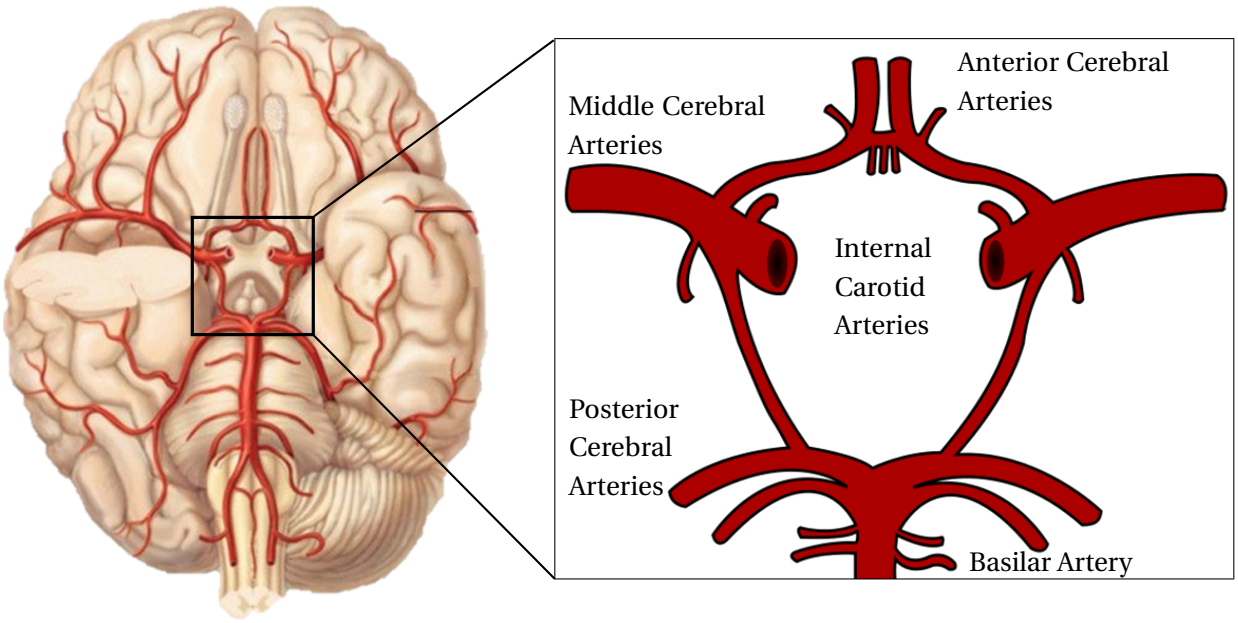

Figure 2.1: Location of Circle of Willis inside the brain, bottom view. All arteries are present on both the left and the right side of the circle, the Basilar Artery excluded.

tunica adventitia is the outer layer of the arterial wall, which consists of irregular fibers which connect the wall to the surrounding tissue [33].

The cells of the endothelium are directly subjected to the Wall Shear Stress (WSS). At a high WSS value, the endothelium cells release nitric oxide (NO). The vessel wall is then dilated so that the vessel diameter increases and the WSS decreases. In this way, blood vessels themselves are capable of adjusting to a range of flow conditions and their WSS values [34]. When the flow rate is increased for longer periods, tears were found in the elastic lamina in the vessel wall [20]. A mathematical description of the WSS will be given in Section 2.2.2. It should be noted that it is likely that abnormalities in the vessel wall are related to the formation of aneurysms [35, 36].

2.1.3. Aneurysms

An aneurysm is a local bulge in the vessel wall, which can have a size ranging from a few millimeters to several centimeters. Most aneurysms are typically located on the aorta or the CoW; where in the latter case they are called intracranial aneurysms. The swelling can cause pressure on surrounding tissue, which can cause pain or loss of functions if the aneurysm is located in the brain. At certain conditions, the aneurysm might rupture. This can cause subarachnoid hemorrhage; a life-threatening loss of blood inside the brain [31]. Patients with a ruptured intracranial aneurysm have a 55 % chance of survival if they arrive at the hospital alive. Most of these patients end up with severe neurological defects [37]. Intracranial aneurysms mostly occur in patients over 40 years old, although they have been found in children as well [3].

It is mentioned by Selimovic et al. [36] that in an existing aneurysm, the tunica media is de-

stroyed, so that the tunica adventitia now is the most important load-bearing layer. This seems to be caused by the fact that a loss of elastin inside the arterial wall induces a repair process. In this process, the elastin is replaced by collagen. In fluid-solid-growth (FSG) models, the assumption that a high WSS results in the degeneration of elastin inside the intima did not result in a saccular aneurysm shape, whereas the application of a low WSS did. At the growth locations it was found that the low WSS values were accompanied by a high WSS-gradient and an unstable flow.

Genesis and growth

Different opinions are present in literature on the genesis and growth of intracranial aneurysms (IA). It is known that most of the aneurysms exist in locations with a 'complex' geometry, such as curves or bifurcations. The most common locations are the downstream MCA bifurcation, the ACA-ACoA bifurcation, or the end of the BA. These locations are subjected to high WSS values [38]. Research on the arterial walls of patients with ruptured intracranial aneurysms shows a decreased wall distensibility and an increased intima-media thickness in the surrounding vessels [35].

The correlation of a low WSS with the growth of an aneurysm is in contradiction with Sforza et al. [21], who say that the locations associated with the genesis of intracranial aneurysms are subjected to a high WSS and a high WSS-gradient. This should weaken the vessel wall, which is caused to bulge out under the pressure of the blood flow. The findings from Sadasivan et al. [38] and Sforza et al. [21] seem to imply that both low and high WSS values have an effect on the genesis of aneurysms, but both in another moment in the time line.

According to White et al. [39], not the spatial WSS gradient but the temporal WSS gradient has a negative influence on endothelial cells in human arteries. This can be defined as oscillations, which will be elaborated on in Section 2.2.3.

Rupture

Several attempts have been made to relate the shape of aneurysms to the risk of rupture [23, 40, 41]. Goubergrits et al. [41] found that multilobed aneurysms are more likely to rupture than spherically shaped aneurysms. Next to that, no differences were found in aneurysm size and average WSS values between the ruptured and unruptured aneurysms. They found that ruptured aneurysms had locations of high WSS in addition to low WSS values in the dome region. Other hemodynamic properties that could predict the rupture sites inside an aneurysm will be dealt with in Section 2.2.

2.2. Hemodynamics

The fluid dynamics that is dealt with when modeling blood flow is called hemodynamics. Blood consists of plasma, red and white blood cells, thrombocytes, and other diluted substances, which all have an influence on the flow behavior of the blood. Therefore, the blood cannot be regarded as a Newtonian liquid, and a model is needed to predict the viscosity under certain shear stress. The most important factor in determining the viscosity is the hematocrit, which is the volume percentage of red blood cells in the blood. Medication, such as blood thinners, can have a drastic effect on the viscosity of the blood. Hitosugi et al. [42] found that

heparin lowers the blood viscosity by almost 50 %. Such a drastic change in viscosity could have interesting corollaries, such as a change in WSS that causes the vessel wall to contract for a longer period of time. This may occur quite often in elderly people who are treated for several diseases.

2.2.1. Fluid flow

To model the behavior of the flow inside the blood vessels, the Navier-Stokes equations are solved numerically. These are given for laminar flow in Euler notation by (2.1) and (2.2).

$$\frac{\partial u_i}{\partial x_i} = 0 \tag{2.1}$$

$$\rho \frac{\partial u_i}{\partial t} + \rho u_j \frac{\partial u_i}{\partial x_j} = -\frac{\partial p}{\partial x_i} + \frac{\partial}{\partial x_j}\left(\mu \frac{\partial u_i}{\partial x_j}\right) \tag{2.2}$$

where u denotes the velocity, ρ the density, p the pressure and μ the dynamic viscosity. The continuity equation (2.1) prescribes that the fluid is incompressible. The time rate of change, convective transport, pressure as a source term and diffusive transport are described by (2.2).

2.2.2. Wall Shear Stress

The definition of the WSS is given in (2.3).

$$\tau_w = \mu \left(\frac{\partial u}{\partial r}\right)_{r=R} \tag{2.3}$$

This quantity is calculated along the wall of the blood vessels. A local high WSS means that the gradient of the velocity in the direction normal to the vessel wall is large. This means that the velocity difference between the center of the vessel and near the wall is large. The time average of the WSS (WSSTA) is often used as a criterion for a localized risk evaluation of aneurysm rupture. This criterion is defined by (2.4).

$$\mathrm{WSSTA} = \frac{1}{T}\int_0^T |\mathrm{WSS}|\,\mathrm{d}t \tag{2.4}$$

where T is the length of a heartbeat.

2.2.3. Oscillatory Shear Index (OSI)

In literature, the OSI is often used to characterize flow patterns in and around aneurysms to predict growth or rupture. OSI is defined in (2.5).

$$\mathrm{OSI} = 0.5\left(1 - \frac{\left|\int_T \vec{\mathrm{WSS}}\,\mathrm{d}t\right|}{\int_T |\mathrm{WSS}|\,\mathrm{d}t}\right) \tag{2.5}$$

This equation was first defined by Ku et al. [26]. The OSI is used to show the locations where the variability of the WSS within one cardiac cycle is large. The cells in the wall then have to endure

large variations in shear stress in a small period of time, which could lead to degradation of the vessel wall. Together with a low WSS time-average (WSSTA) value, there is a high risk of aneurysm rupture [1, 27, 30].

2.2.4. Wormersley flow

Due to the pulsating nature of blood flow, a parabolic velocity profile is often not the right approximation for the blood flow inside blood vessels. To determine the nature of the velocity profile, Womersley [43] described a dimensionless number that was a combination of the Reynolds number and the Strouhal number; the Wormersley number (α). Defined by (2.6).

$$\alpha = R\sqrt{\frac{\omega}{\nu}} \tag{2.6}$$

Where R is the radius of the artery, ω is the angular frequency of the pulsating flow and ν is the kinematic viscosity of blood. The number describes the relation between transient inertial forces and viscous forces. When the number is low ($\alpha < 1$), the velocity profile between pulses develops to a parabolic profile, when the value is high ($\alpha > 10$), the profile approximates a plug flow profile [44].

Blood in the cerebral arteries has Wormersley numbers between $\alpha \approx 1.4$, for small blood vessels and a low heartbeat rate, and $\alpha \approx 4$ for larger vessels and a higher heartbeat rate. This means that the velocity profile has a shape that lies in between the parabolic profile and a plug profile.

3

Numerical Methods

In this Chapter, the methods with which the equations (2.1) and (2.2) are solved, will be explained. Next to that, the methods of preparing the geometry for meshing, the meshing itself, the mesh sensitivity study and the time resolution will be touched upon.

3.1. Models and Convergence

All simulations are done with Fluent 17.1 from ANSYS [45]. This Section covers the methods used by this simulation package to solve the equations (2.1) and (2.2). According to Khan et al. [46], the numerical methods used in a hemodynamic simulation are essential to the simulation's accuracy. The use of second-order methods instead of first-order methods is crucial for accuracy and these will, therefore, be used in this study.

Blood flow in the CoW can be modeled as a low-speed incompressible flow. Consequently, the choice has been made for the pressure-based solver. The governing equations are discretized and a Finite-Volume approach is used to solve these equations for each control volume. The coupled governing equations are decoupled and solved in a segregated manner. The SIMPLE (Semi-Implicit Method for Pressure-Linked Equations) algorithm uses a combination of pressure corrections and velocity to satisfy the discrete governing equations [45, 47]. The models and settings that have been used are listed in Table 3.1

Table 3.1: Solver settings used in Ansys FLUENT

Setting	**Value**
Physics Solver	Pressure based
Pressure	Second Order Upwind
Momentum	Second Order Upwind
Gradient	Least Squares Cell Based
Velocity and Pressure coupling	SIMPLE
Time step	Second order Implicit
Residual Threshold (Absolute)	10^{-5}

3.2. Boundary conditions

The wall of the geometry has been modeled as a rigid wall with no-slip boundary conditions. This approach has been used in several studies [9, 13, 18].

3.2.1. Inlet

The inlet boundary conditions are provided on the BA, RICA and LICA. In the first simulations, a parabolic velocity profile following a heartbeat was used [13]. The data for these profiles was provided by the AMC, where the average flow velocity was measured for 12 time steps in one heartbeat. A Fourier fit of these data points makes it possible to define this profile for all time steps in the measured heartbeat. This Fourier fit can be found in Figure 3.1.

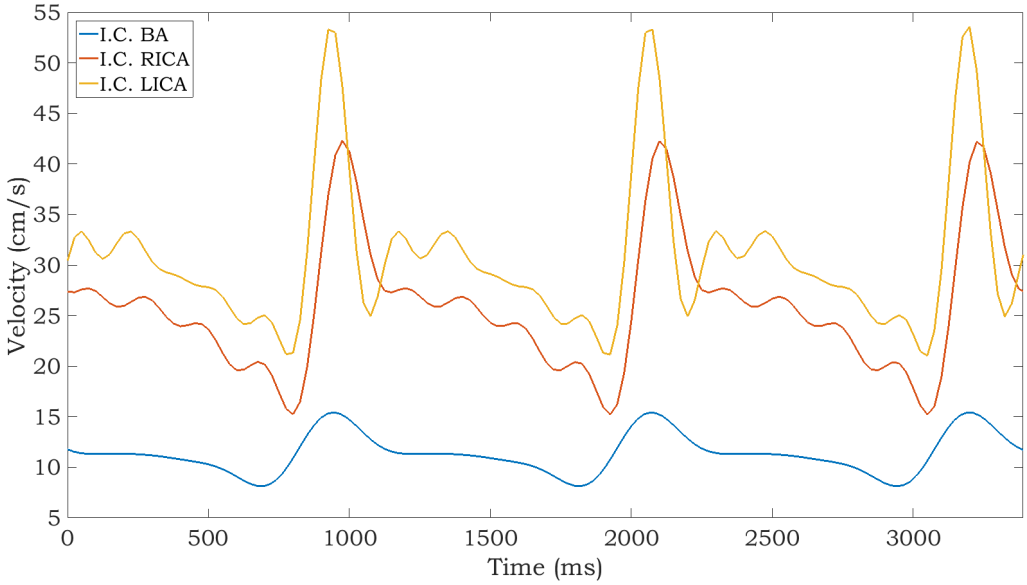

Figure 3.1: Fourier fits for the inlet boundary conditions for the healthy CoW simulation

The influence of the initial conditions is verified by comparing WSS values at several time-instances in the heartbeat after one, two and three heartbeat cycles. The result of this simulation can be found in Figure 3.2. In this Figure can be seen that the WSS in the first heartbeat shows a large difference (> 50 % difference) from the WSS values in the second and the third (< 1 % difference). This means that the initial conditions need at least one cardiac cycle to be mitigated. From this can be concluded that at least two heartbeat cycles should be simulated before data can be extracted and conclusions can be drawn from the results.

Flow Profiles

The influence of the enforced velocity profile at the inlet was studied by a simulation on a healthy CoW geometry. In literature, the Wormersley flow profile is mentioned as the desired inlet velocity profile. The extreme shapes of the Wormersley profile for the Wormersley numbers that occur in the CoW are a plug flow profile and a parabolic profile. Both these profiles have been simulated so that the significance of their difference can be determined. The difference between these two models is negligible. Because the use of cylindrical extrudes at the

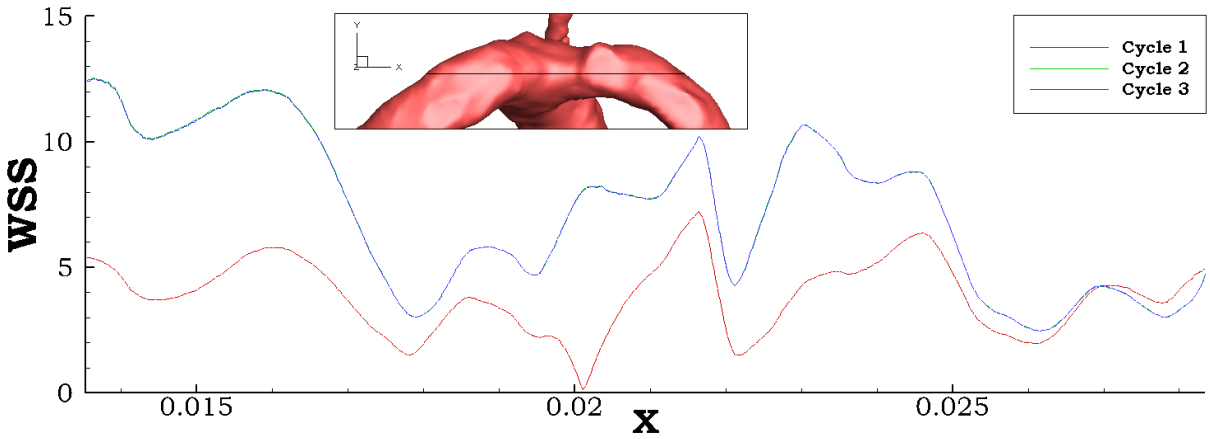

Figure 3.2: Wall Shear Stress values of a line along the surface at $y = 0.019$ m at times in the first, second and third simulated heartbeat. The green and blue lines lay on top of each other.

inlets of the geometry, the plug flow profiles develop to parabolic profiles before they enter the actual blood vessel. Table 3.2 shows the Wormersley numbers for all arteries in the CoW calculated with equation (2.6). The area is obtained from the geometry, from which the radius is calculated. The angular frequency of the heartbeat is extracted from the Fourier fit on the heartbeat data. The low values of α suggest that a parabolic inlet profile is sufficient to model the blood flow in this CoW.

Table 3.2: Wormersley numbers in all arteries inside the CoW.

Artery	BA	LICA	RICA	LACA	LMCA	LPCA	LSCA	RACA	RMCA	RPCA	RSCA
α	2.75	2.97	3.09	2.09	2.40	1.84	1.33	1.88	2.02	1.55	0.90

3.2.2. Outlet

The boundary conditions at the outlet are provided as a targeted mass flow that is a fraction of the total inflow in the system. Several methods are known to calculate these fractions so that the simulated flow is as realistic as possible. The first way to calculate the outflow fractions is to use the data provided by the MRI scans themselves. It is found, however, that the sum of the mass flow at the inlets is not always equal to the mass flow at the outlets. This means these values can only be used as guidelines.

A second way to specify the mass flow is with Murray's law, which describes a certain outflow as a fraction of the mass flow at the inlets. The law prescribes a relation between the ratio of the volumetric flow rate Q and the ratio of the upstream and downstream vessel radii (3.1) [48].

$$\frac{Q_{out}}{\sum Q_{in}} = \frac{R_{out}^3}{\sum R_{in}^3} \tag{3.1}$$

Instead of this calculation, the outflow mass fraction per outlet can also be calculated with the areas of the blood vessels (3.2).

$$\frac{Q_{out}}{\sum Q_{in}} = \frac{R_{out}^2}{\sum R_{in}^2} \tag{3.2}$$

The areas of the blood vessels were measured by MRI for each inlet and outlet so that the outflow mass fraction could be calculated.

Both equations (3.1) and (3.2) were implemented as outflow boundary conditions to study their influence on the total flow field and the resemblance to the MRI velocity results. It turned out that equation (3.2) gave the best results, when the areas measured by the MRI scanner were used. In this way, the outflow conditions were calculated from the total inflow. The fractions used for the healthy CoW model are given in Table 3.3. These were implemented by a User Defined Function (UDF), of which the first version was created by Perinajová [13].

Table 3.3: Imposed outflow fractions for the healthy Circle of Willis simulation.

Outlet artery	LACA	LMCA	LPCA	LSCA	RACA	RMCA	RPCA	RSCA
Flow fraction	0.12	0.25	0.09	0.05	0.11	0.29	0.07	0.02

3.3. Preparing the geometry

In the process of MRI scanning, there is always a trade-off between the spatial and temporal resolution. This data set has a time resolution of 12 time steps, and the MRI data has a spatial resolution of 0.5 mm in three directions. Therefore the surface has to be smoothed in order to use the geometry for CFD simulations. To do this, the Vascular Modeling Toolkit is used. The Vascular Modeling Toolkit (VMTK) is a Python-based program that lets one smooth the often rough images that are produced by MRI scans [49]. The geometry of the arteries is further prepared for use in CFD models by adding extrusions and caps to the inlets and outlets of the vessel system and by enhancing the surface so that the surface can be used for mesh generation. In Figure 3.3 the result of the smoothing and extrusion of the geometry is shown. The VMTK code used for these manipulations can be found in Appendix C.

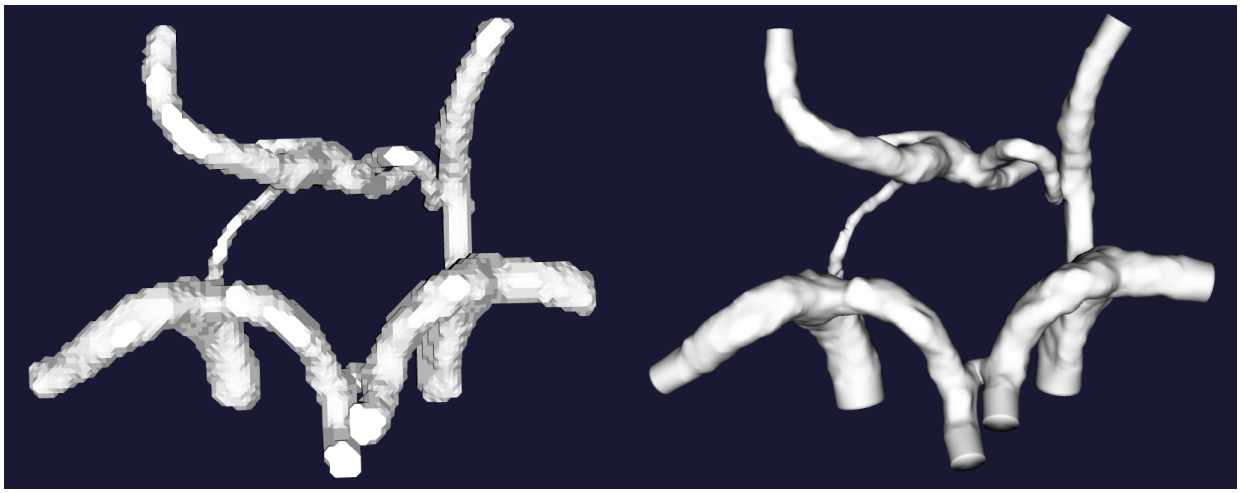

Figure 3.3: The results of the VMTK smoothing: on the left side the raw MRI image is shown, on the right side the exportable geometry.

3.4. Mesh

After preparation of the geometry, the mesh is generated using the Ansys ICEM mesher. A polyhedral mesh is made with a boundary prism cell layer of 6 cells. Refinement is used along corners and in small arteries. The mesh is visualized in Figure 3.4 with a zoom on the BA, the LPCoA and the RPCoA-RMCA shoulder. In Table 3.4 the largest and smallest mesh sizes are listed.

Table 3.4: Minimal and maximal element sizes of CoW mesh

Element	**Volume** (mm^3)	**Length scale** (mm)
Smallest	$4.7165 \cdot 10^{-8}$	0.00361
Largest	$4.1398 \cdot 10^{-3}$	0.161

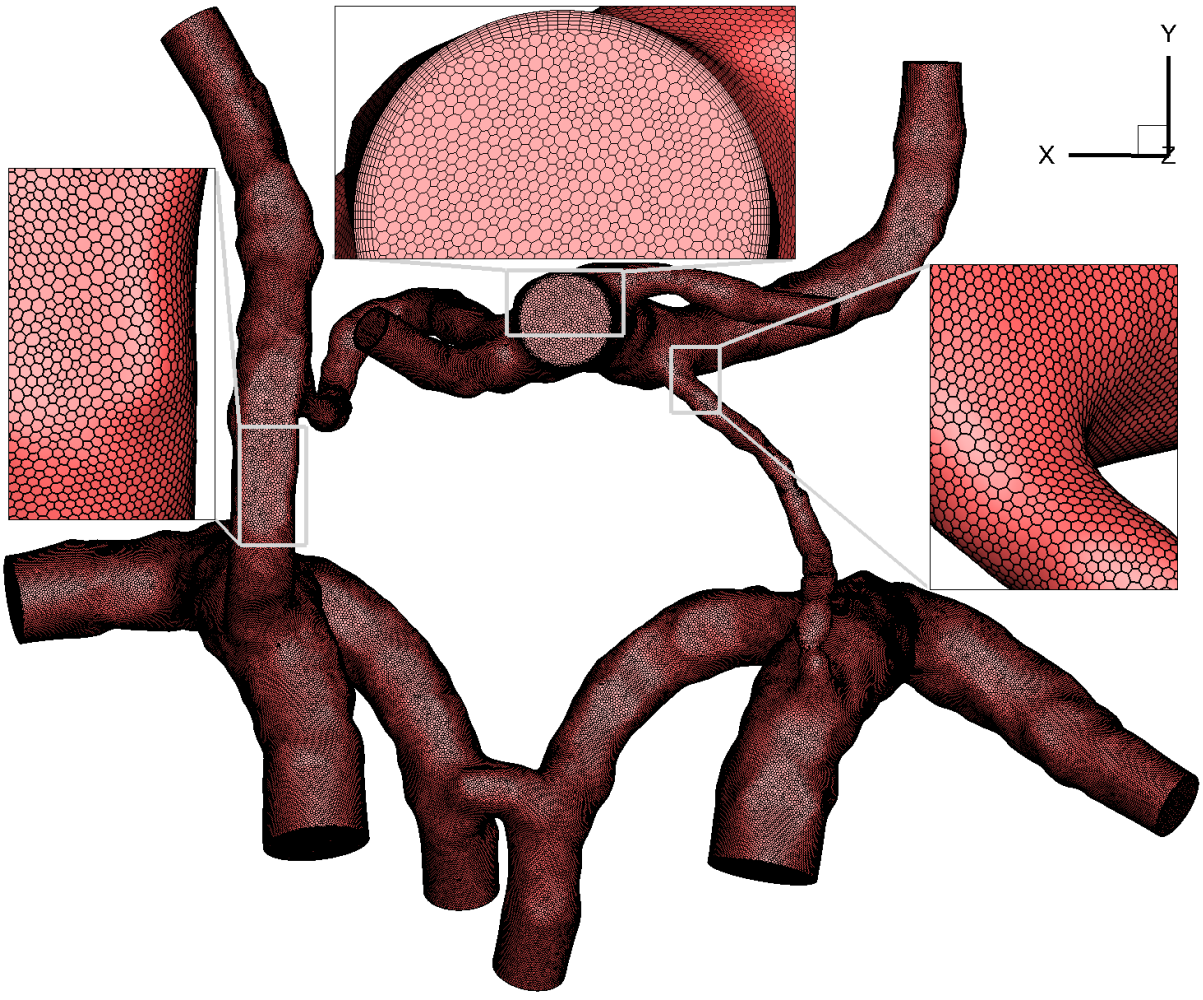

Figure 3.4: Visualization of the mesh (3M cells) with a zoom on the BA, the LPCoA and the RPCA-RPCoA shoulder

3.4.1. Mesh sensitivity

To make sure that the solution found by ANSYS Fluent does not depend on the mesh size, several simulations were performed to map the changes in the solution due to changes in

mesh size. The mesh sizes for the mesh sensitivity study are listed in Table 3.5. The results of the simulations done with the coarse, medium and fine mesh are given in Figure 3.5. In this Figure the WSS on a line on the surface is plotted. The Figure shows that there is a small difference between the coarse, medium and fine mesh. Because of this small difference, for the following calculations, a mesh with at least 2.5 million polyhedral cells will be used.

Table 3.5: Mesh sizes, resolution and the relative error of all meshes of mesh sensitivity study

Mesh	**1**	**2**	**3**
Size (tetrahedral)	9M	17M	28M
Size (polyhedral)	2.5M	4.5M	6.3M
WSS average (Pa) on line $y = 0.019$ m	19.1584	19.2329	19.5079
Error relative to fine mesh	1.79 %	1.41 %	-

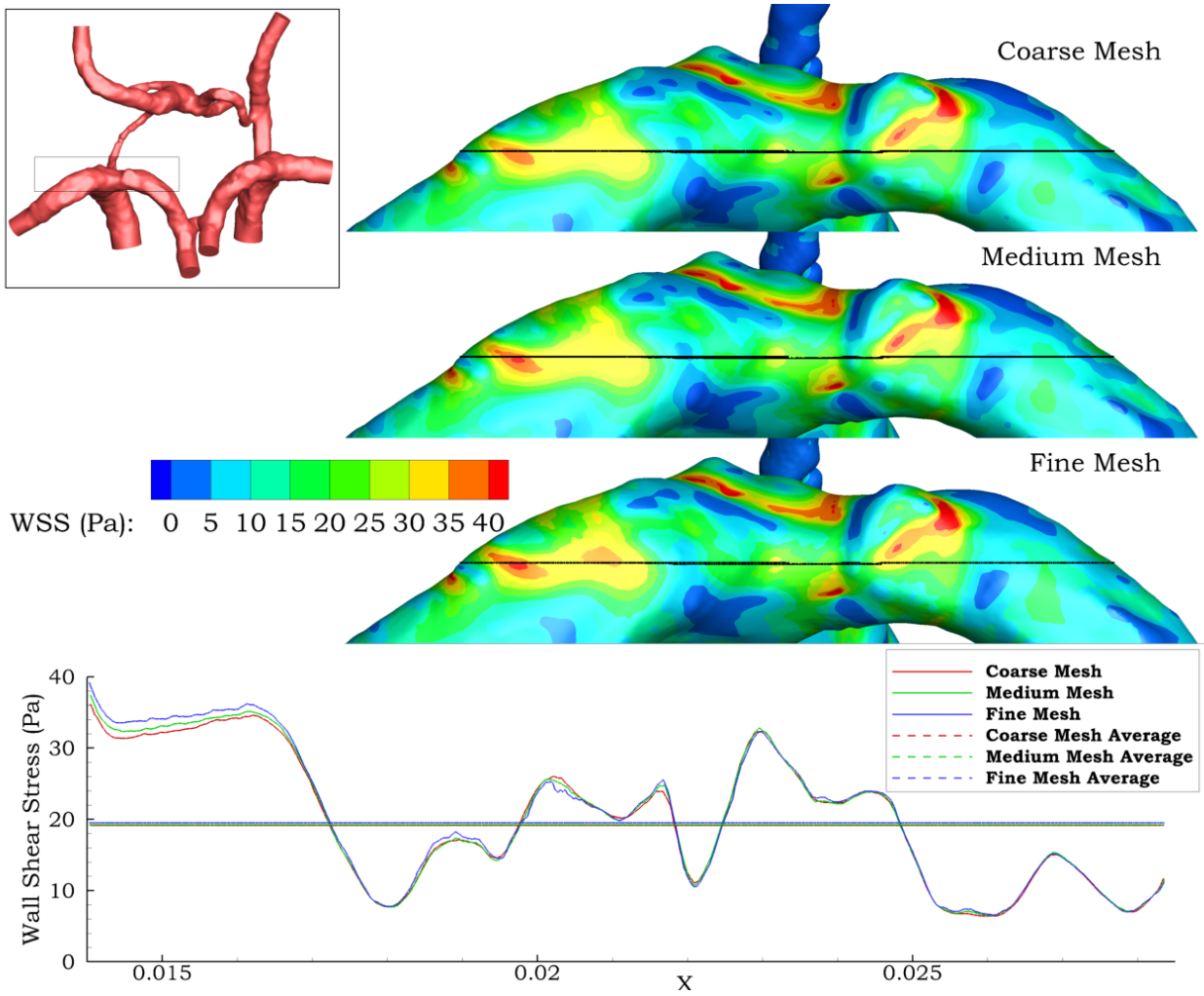

Figure 3.5: WSS plot at the surface of the CoW at $y = 0.019$ m

3.5. Material properties

The properties of blood have been used as material properties in all CFD simulations. The density ρ is taken as 1060 kg m^{-3}. For the viscosity the Carreau-Yasuda model is used, which was provided by Perinajová [13]. This model is described by equation (3.3) and the parameters of this model are given in Table 3.6. This model results in non-Newtonian properties so that the blood behaves as a shear thinning liquid.

$$\mu(\dot{\gamma}) = \mu_\infty + (\mu_0 - \mu_\infty)\left(1 + (\dot{\gamma}\lambda)^a\right)^{\frac{n-1}{a}} \tag{3.3}$$

where $\dot{\gamma}$ is defined as the strain rate.

The influence of this model has been verified by comparing simulations with the Carreau-Yasuda viscosity model with simulations with a constant viscosity of 0.0035 Pa s. For both the systole and the diastole, the velocity values are plotted. These results can be found in Figure 3.6. These plots show that the velocity differs with a maximum of 0.025 m s^{-1}, which is a relative maximum difference of around 5 %.

The WSS values in both simulations show little difference (< 5 %), which can be explained by the fact that the viscosity model does not have much influence near the wall, as the velocities

Table 3.6: Fitted values for the Carreau-Yasuda viscosity model [13]

Parameter	Value
μ_0	213.1
μ_∞	3.14
λ	50.2
a	0.8588
n	0.331

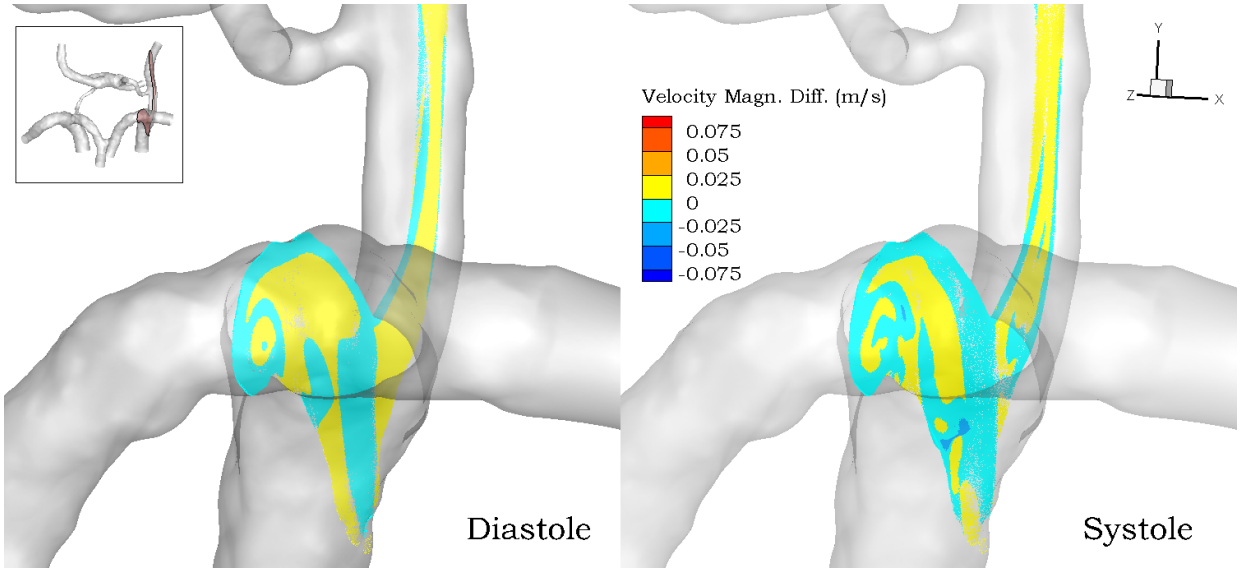

Figure 3.6: Velocity difference between Carreau-Yasuda model and constant viscosity. Plot originating at a slice at x = 0.045 m for both the diastole and the systole of the heartbeat.

are small at those locations. The Carreau-Yasuda model will be used in all future calculations. This study suggests that if the assumption of constant viscosity would be made, the effect would be small.

3.6. Temporal Resolution

The temporal mesh was validated as well. Depending on the size of the time steps, numerical diffusion affects the temporal mesh. Khan et al. [46] concluded that the temporal mesh size can have a large influence on numerical results of unstable hemodynamic simulations. Therefore after establishing a minimal spatial mesh size, the minimal temporal resolution has been investigated. For that, three simulations were performed with time steps of Δt = 0.01 s, Δt = 0.001 s and Δt = 0.0001 s. The static pressure and the velocity magnitude have been probed at three points: inside the BA, at the shoulder of the LICA and at the end of the RMCA. Figure 3.7 shows the results for the three different time steps in the temporal resolution. The pressure data of the largest Δt differs from the smaller Δt in all three locations (< 3 %). The velocity measurements are similar for all resolutions (difference < 1 %). From this can be concluded that a time step of 0.001 s is necessary and sufficient to perform accurate simulations.

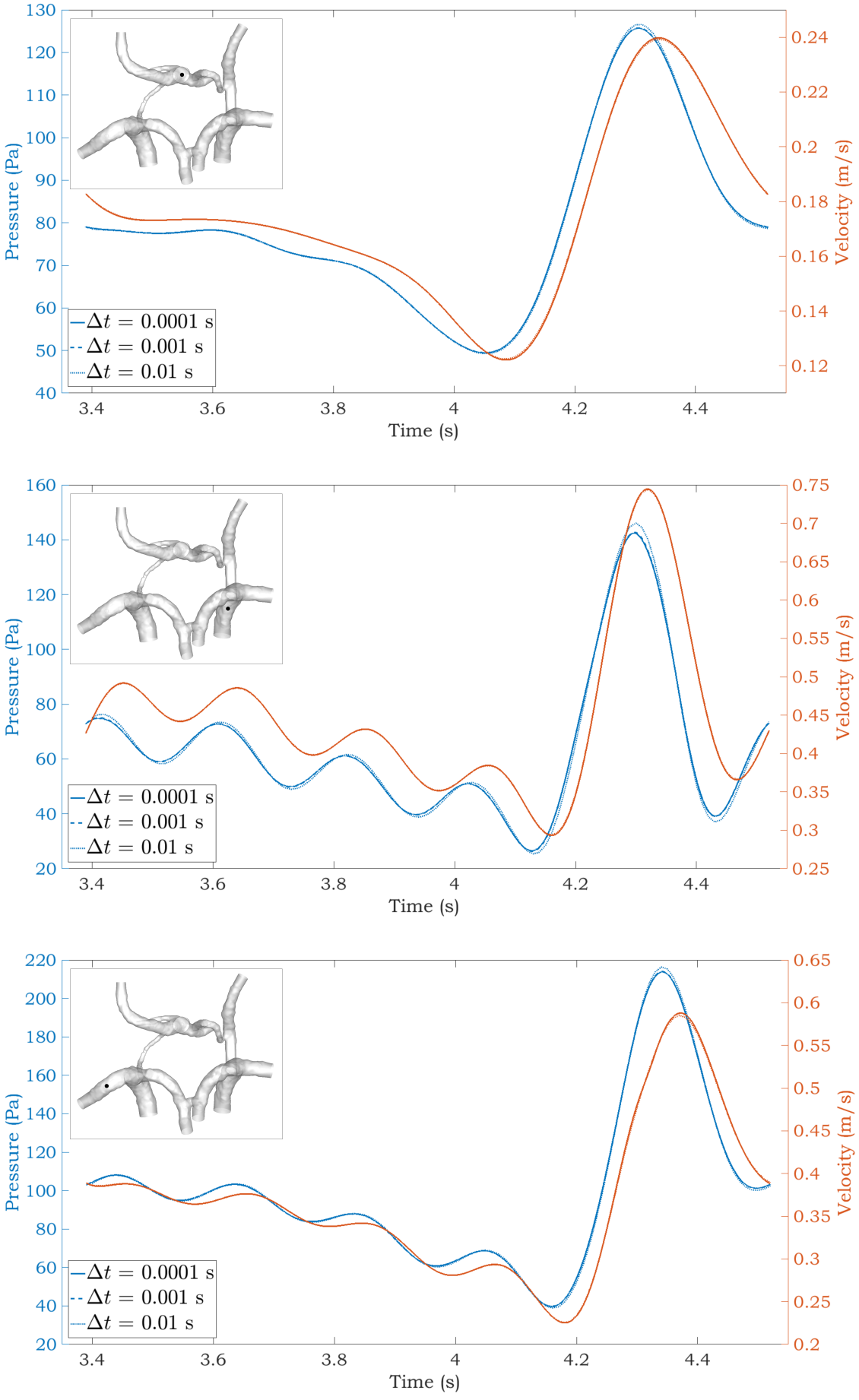

Figure 3.7: Results of the temporal resolution measurements at three locations for the static pressure and the velocity magnitude.

4

Healthy Circle of Willis

This Chapter describes the similarities and the differences that are found when comparing MRI data to CFD simulations, to extend the results provided by Perinajová [13]. It will also give a critical view on the resolution of MRI measurements. Afterward, the implication of different blood viscosity values is discussed.

4.1. Geometry

The healthy CoW geometry is obtained from the 7T MRI scanner from the Academic Medical Center in Amsterdam. The geometry with the appointed names of the arteries can be found in Figure 4.1.

4.2. Evaluation of MRI data

The measurement data that have been obtained from the AMC in Amsterdam have to be post-processed to visualize the data and draw conclusions from the comparison with the CFD results. The MRI data is obtained as a 5D matrix containing three coordinates, their velocity values, and time. The spatial resolution is 0.5 mm, the temporal resolution is 12 time steps per heartbeat. This data is processed by a Matlab script that reads the 5D velocity and WSS data and displays it. This script can be found in Appendix B.

In addition to this, WSS values are directly calculated from these velocity measurements, using the velocity gradients. This means that the velocity data, that already shows some error, has to be interpolated to find WSS values. In some arteries only two or three measuring points in a cross-section are present. If one of these points is noisy, the WSS calculations made with these data points is unreliable.

4.2.1. Flow properties MRI data

To make an analysis of the similarities between CFD and MRI, it is important to investigate the imperfections of the MRI data as well. Figure 4.2 shows the velocity magnitude extracted from the MRI velocity data with a zoom on the RMCA. The slices are visible in the y-direction

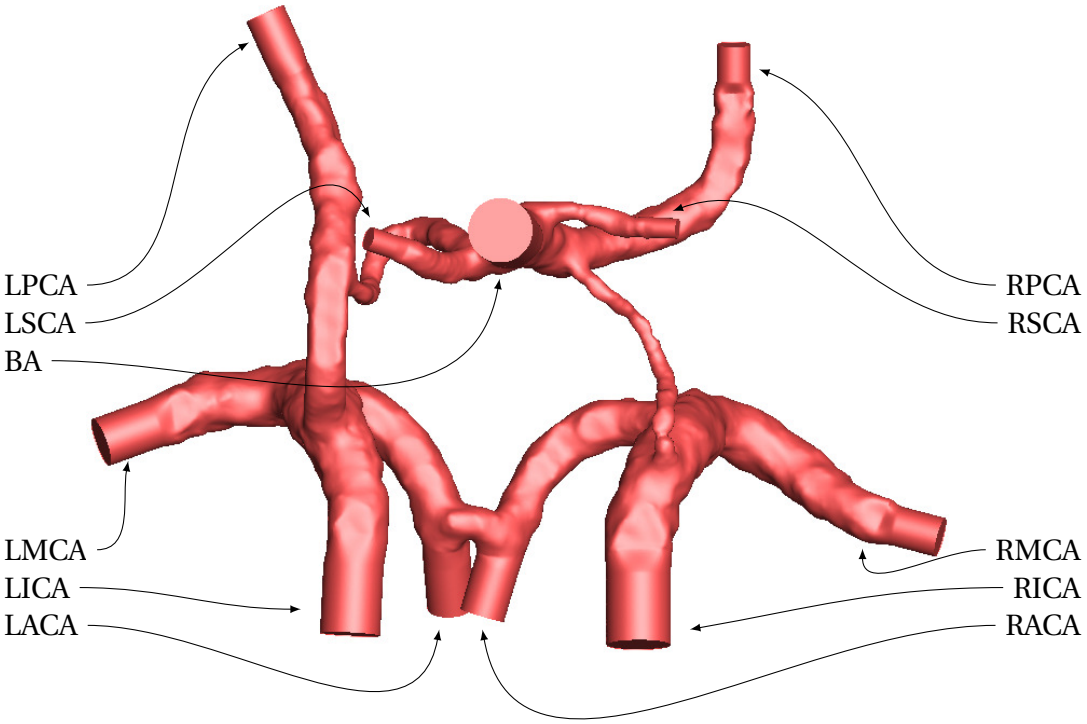

Figure 4.1: Bottom view of a patient-specific geometry of the Circle of Willis

so that the geometry is rotated 90 degrees. To find out whether the comparison with CFD is valid, a continuity evaluation has been done on the RMCA, the RPCoA and the BA. In at least 7 slices in each of these arteries, the velocity normal to the plane has been investigated. In this evaluation, the average normal velocity was multiplied by the number of pixels and the size of a pixel to obtain a volumetric flow equivalent. These flows were compared in all slices of each artery. This evaluation was done for three time-steps. The Figure shows that the volumetric flow rate is not equal through each plane, which should be the case.

It was found that in the RPCoA the absolute errors were smallest ($\pm$ 0.2 mL s^{-1}) but the relative errors were up to 95 % with respect to the median. This high percentage was due to the low absolute velocities. For the BA the errors were smallest, the overall error was in the order of 5 %. The RMCA had relative errors of around 10 %. The full table with all values can be found in Appendix A.1.

4.3. Results: Comparison CFD-MRI

For an MRI-obtained geometry of a Circle of Willis simulations have been performed with initial and boundary conditions provided by MRI measurements. In this section, these measurements are compared with the results of the simulations for velocity measurements and WSS values.

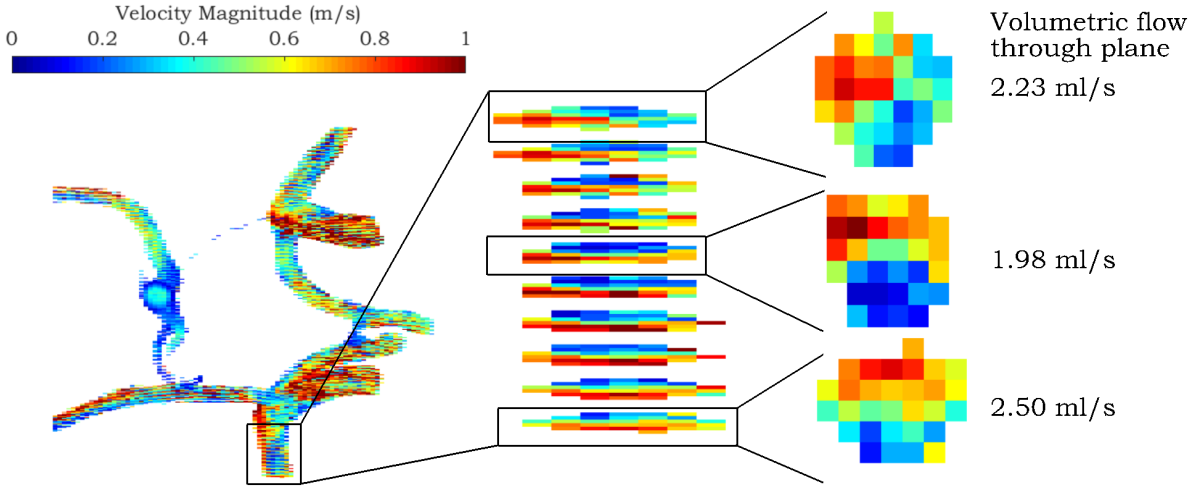

Figure 4.2: Flow measurements from MRI scanner in their original resolution. Three slices of the RMCA have been zoomed in on to show the discontinuity between the planes in the systole phase.

4.3.1. Velocity measurements

The comparison of MRI flow velocity data and CFD velocity data is a follow-up on the research done by Perinajová [13]. In Figure 4.3 the comparison of the velocity magnitude in several slices of the CoW can be seen for both the systole and the diastole. In both images the overall velocity magnitude is similar. During the systole, the MRI data shows some high values that are not present in the CFD image. These high values are probably caused by noise in the MRI data. In the systole image can also be seen that the velocity at the wall is not necessarily measured to be zero. This can be the case due to averaging over a voxel in the MRI data.

Figure 4.4 shows one slice of the MRI measurements with the corresponding CFD results. The Figure shows that the global characteristics of the flow are mimicked well by the CFD simulation. A few voxels from the MRI measurements show unexpectedly high velocities. These red spots can occur because of measuring errors in the MRI data.

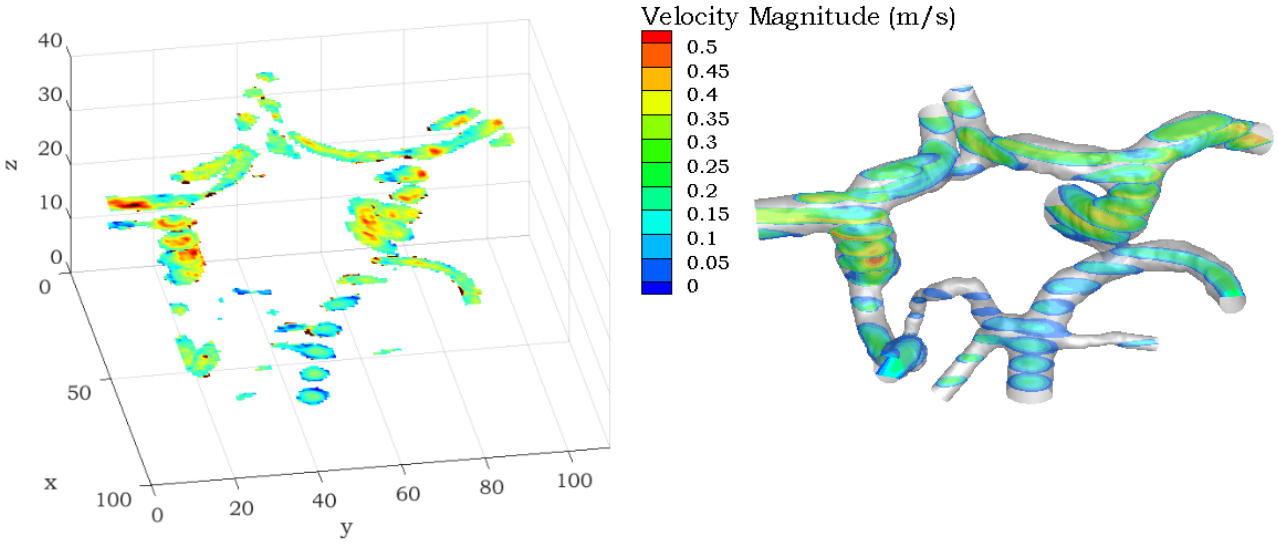

(a) Diastole

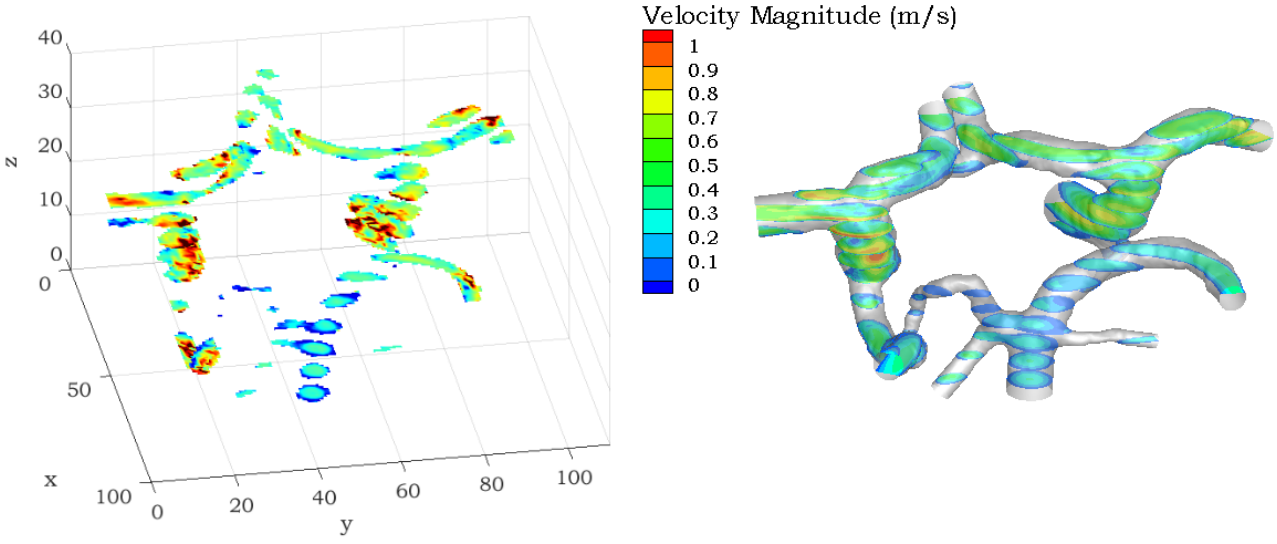

(b) Systole

Figure 4.3: The comparison of the velocity magnitude in several slices of the MRI data (left) with CFD data (right) for the diastole ($0.66T$) and systole ($0.83T$) phase of the cardiac cycle. The xyz-coordinates of the MRI data denote voxels.

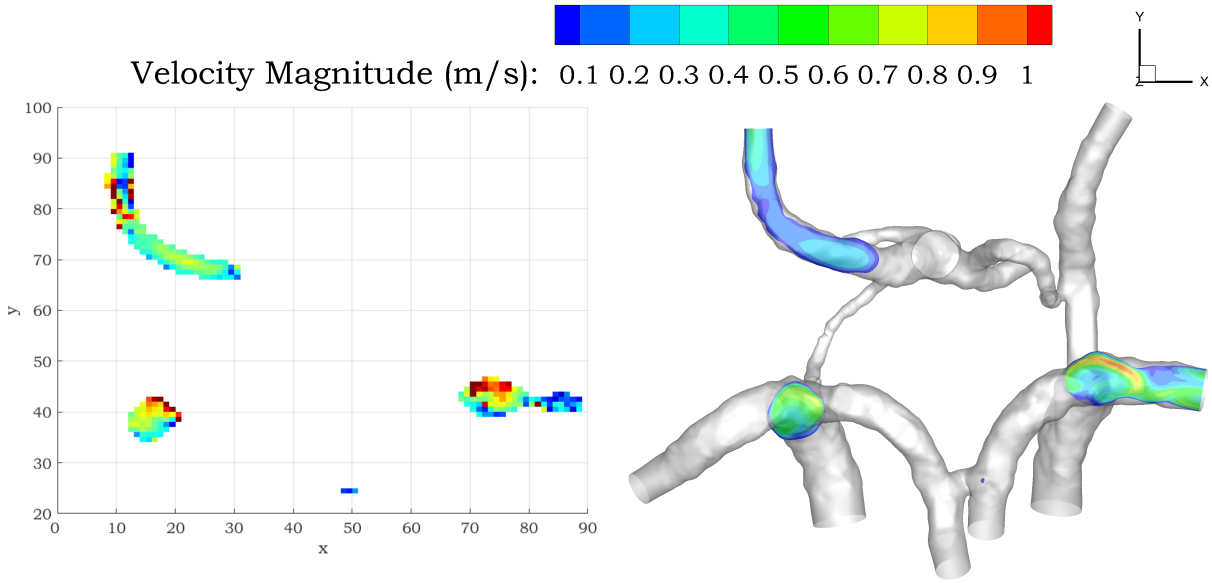

(a) Plane comparison CFD-MRI for the 25th MRI plane in the z-direction during systole

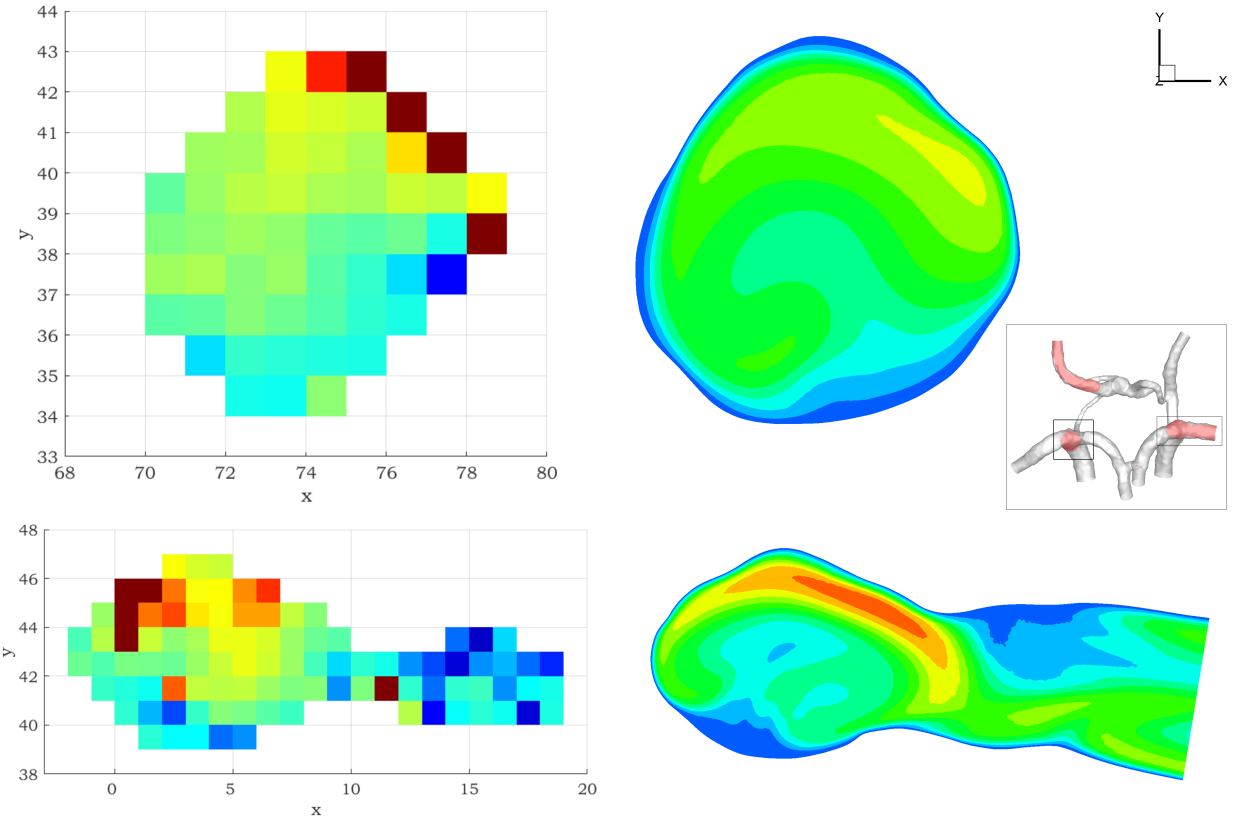

(b) Zoom on parts of the 25th plane, comparison between MRI (left) and CFD (right).

Figure 4.4: The comparison of the velocity magnitude in a z-plane of the MRI data (left) with CFD data (right) for the systole ($0.83T$) phase of the cardiac cycle. The xyz-coordinates of the MRI data denote voxels.

4.3.2. Wall Shear Stress

In Table 4.1 the average and maximum values of the MRI data and the simulations can be found. The maximum value of the WSS in the MRI data is higher for the diastole than for the systole. This is not expected and can be the result of the calculations of the WSS that depend on the relatively low resolution of the gradients of the velocity data. If so, this means that displaying the WSS data normalized according to its maximum value can lead to biased plots. The characteristics of the high and low WSS values can, however, be identified when this displaying method is used.

The WSS values of the MRI data and the CFD simulations are compared in Figure 4.5, where the values are normalized by their maximum value in that time step. Because both the systole and the diastole MRI data have been normalized by a number with the same order of magnitude, the difference between the two time steps is very large. In the CFD data, however, both time steps have been normalized by two numbers that differ almost an order of magnitude so that the characteristics of these plots are very similar. This is as expected because the flow characteristics do not inherently change in shape as much as in magnitude during the cardiac cycle. The locations with the high WSS values in the CFD images occur in regions where a high flow velocity is present. This explains the elevated WSS in the MCAs with respect to the PCAs, as the MCAs generally have a higher flow velocity. This is due to the high flow velocity in the ICAs, the mother artery of the MCAs, with respect to the BA.

When the MRI and the CFD data are compared in the diastole, a slight similarity in the flow characteristics can be found. The RPCA has a region with elevated WSS values and in the both MCAs the WSS values in the MRI are heightened as well, although this is more visible in the CFD simulation than in the MRI data. In the systole the same regions with elevated WSS values can be found in the CFD image, and in the MRI data these regions are also subjected to a high WSS. This means that local geometry is more important for the WSS variations, as these variations are the same in several time instances of the cardiac cycle.

Table 4.1: Average and maximum WSS values for diastole and systole in CFD and MRI

	Avg WSS (Pa)		**Max WSS (Pa)**	
	MRI	CFD	MRI	CFD
Diastole	1.72	1.91	24.72	20.4
Systole	3.97	5.24	17.82	92.5

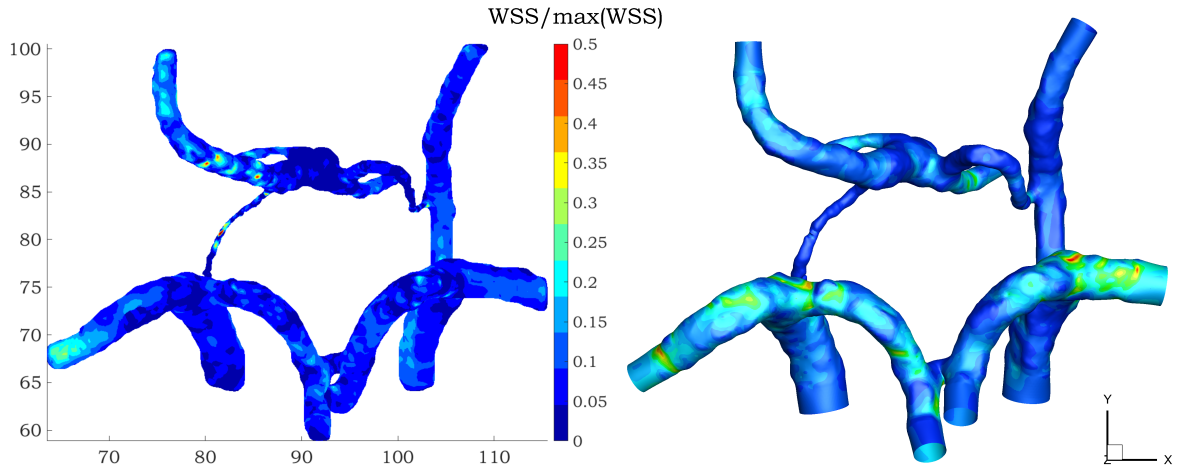

(a) Diastole

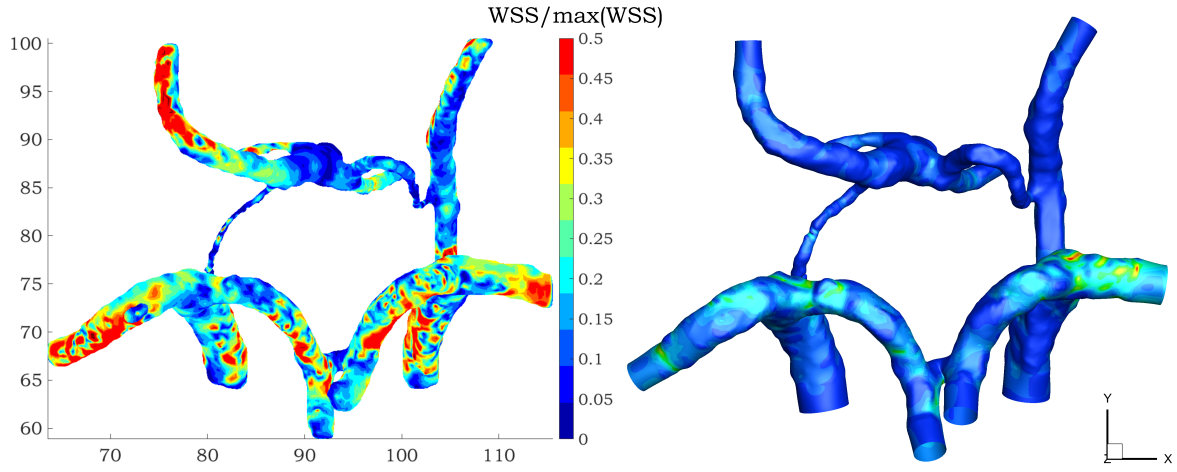

(b) Systole

Figure 4.5: The comparison of the WSS on the z-plane of the MRI data (left) with CFD data (right) for the diastole ($0.66T$) and systole ($0.83T$) phase of the cardiac cycle. The xyz-coordinates of the MRI data denote voxels.

4.4. Blood thinners

The effect of medicinal blood thinners on the properties of the flow was simulated with a constant viscosity of 0.025 Pa s ([42]) with probes on the BA, the LICA and the RMCA. The coordinates of these probes are: (0.0317, 0.033, 0.006) for the BA, (0.044, 0.016, 0.009) for the LICA and (0.012, 0.016, 0.0195) for the RMCA. Due to the only slight difference in the simulations with a constant viscosity and a viscosity model (Section 3.5), a constant viscosity has been used.

In Figure 4.7 the static pressure en velocity data on probed locations in the BA, LICA and RMCA are given. In these figures, two heartbeats of period $T = 1.13$ s are shown for the data of the model with and without blood thinners. For all three locations, the static pressure of the normal blood is higher than the static pressure with blood thinners. Both simulations have the same enforced velocity profile, so with a lower viscosity, the pressure is indeed expected to be lower. In the BA neck and the RMCA this difference is about 15 Pa, in the LICA the difference is smaller because that probed point is closest to an inlet.

For the velocity, the difference between normal blood and blood with a lower viscosity is smaller, but noticeable for the BA and the RMCA. Again, the difference in the LICA is less visible because the probing point is closer to the inlet where similar velocity profiles are enforced. The difference in velocity is expected because a lower viscosity enforces a higher velocity due to less friction.

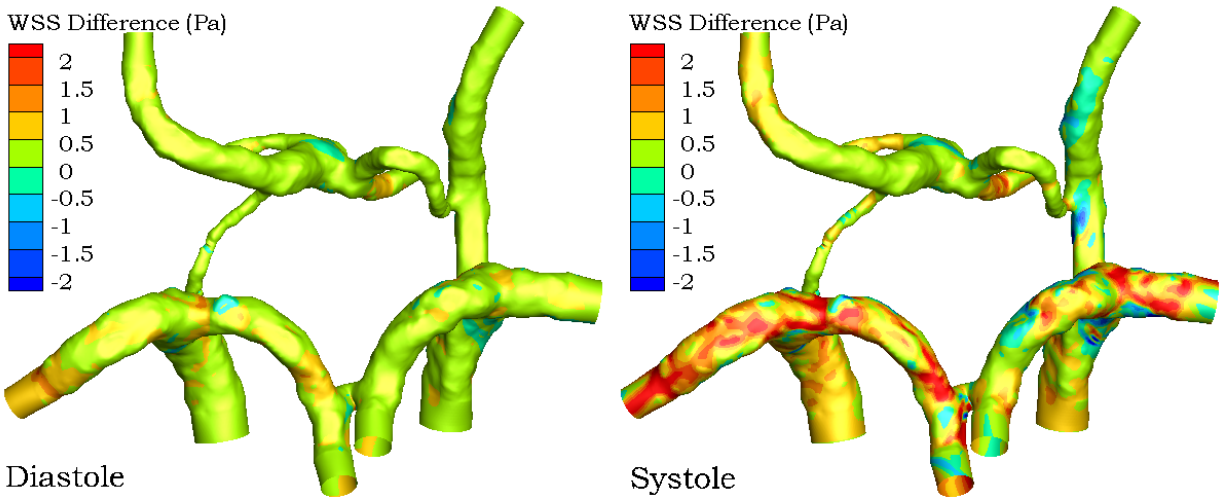

Figure 4.6: The difference in WSS between the normal case and the blood thinner case for the diastole ($0.64T$) and systole ($0.87T$) phase of the cardiac cycle.

Next to a comparison of static pressure and velocity, the WSS has been compared as well. In Figure 4.6 the WSS values for both cases are shown for the diastole ($0.64T$) and systole ($0.87T$). In most locations, the WSS values are lower for the simulation with blood thinners, although the difference between the two cases is small. In Figure 4.6 this can be observed as a small difference in the WSS pattern in the LMCA and RMCA in the diastole phase and in the RPCA in the systole phase.

This means that a lower viscosity is correlated with a lower WSS. When a lower WSS is indeed a cause of the growth of aneurysms, this could be listed as an extra risk when using blood thinners.

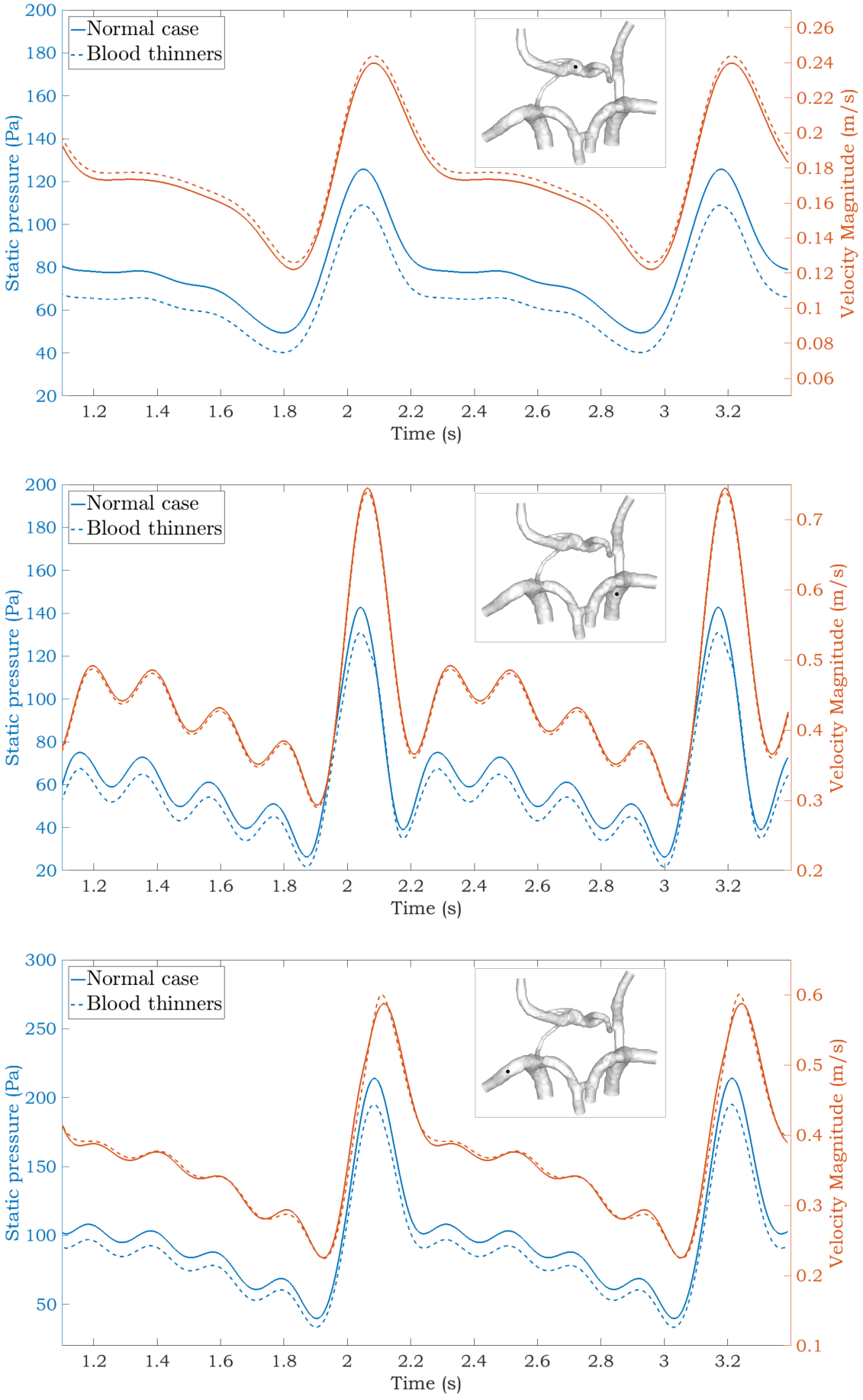

Figure 4.7: Results of the use of blood thinners for the static pressure and the velocity magnitude measured at three locations.

4.5. Discussion

MRI scanners are a very expensive part of hospital equipment. New research techniques try to find ways to reduce the time spent in an MRI scanner and to use the obtained data to the fullest. This research makes a comparison between flow measurements from a 7T MRI scanner and CFD simulations that have been performed with MRI measurement data. For the velocity fields, the agreement is good. The WSS values differ in magnitude, but the locations with high and low WSS are similar for CFD and MRI. This means that the hemodynamics of the system is well-captured by CFD.

The exact cause of the development of aneurysms is still unknown, but is likely a combination of multiple factors. One of these factors is a low WSS value, which causes the endothelial cells to release NO. NO causes the muscles in the vessel wall to contract, to increase the blood velocity and thus increase the WSS. People that use blood thinners have blood with a lower viscosity, which decreases the WSS and increases the maximum velocity. This means that more NO is released, and the blood vessels are contracted more often. Eventually, this could lead to wear of the muscle cells in the vessel wall and this might encourage the growth of aneurysms.

5

CoW with Aneurysm

The second geometry that was obtained from the AMC was a CoW with a saccular aneurysm with a well-defined neck on the downstream RMCA. This geometry is shown in Figure 5.1. In addition to that, the LPCoA was missing, which cuts off the connection between the BA and the LICA.

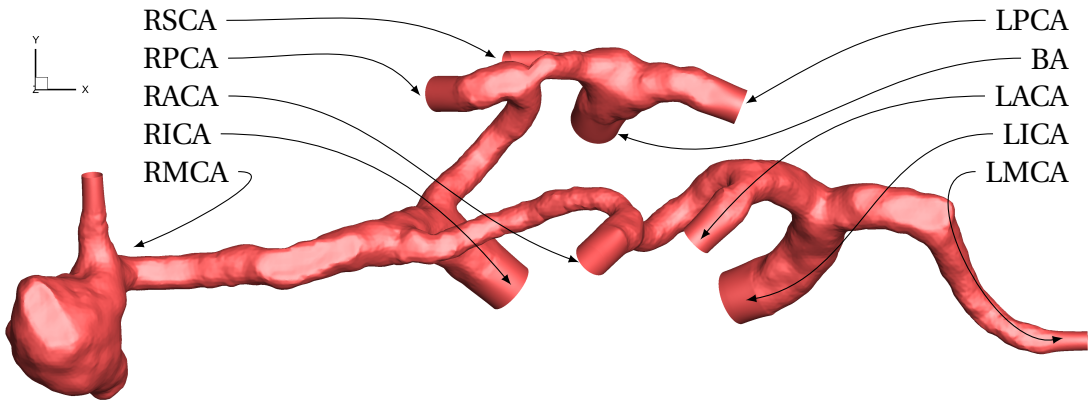

Figure 5.1: CoW with an aneurysm on the RMCA.

5.1. Methods

In this section, the simulation process is explained as an addition to Chapter 3.

5.1.1. Mesh

This geometry was meshed with 10 million cells in the tetrahedral mesh and 2.8 million polyhedrals. Both the polyhedral and the tetrahedral meshes have been simulated to prove that they give similar results. Furthermore, a finer mesh of 20 million polyhedral cells has been simulated as well. Figure 5.2 shows the values of the WSS on the wall of the RMCA.

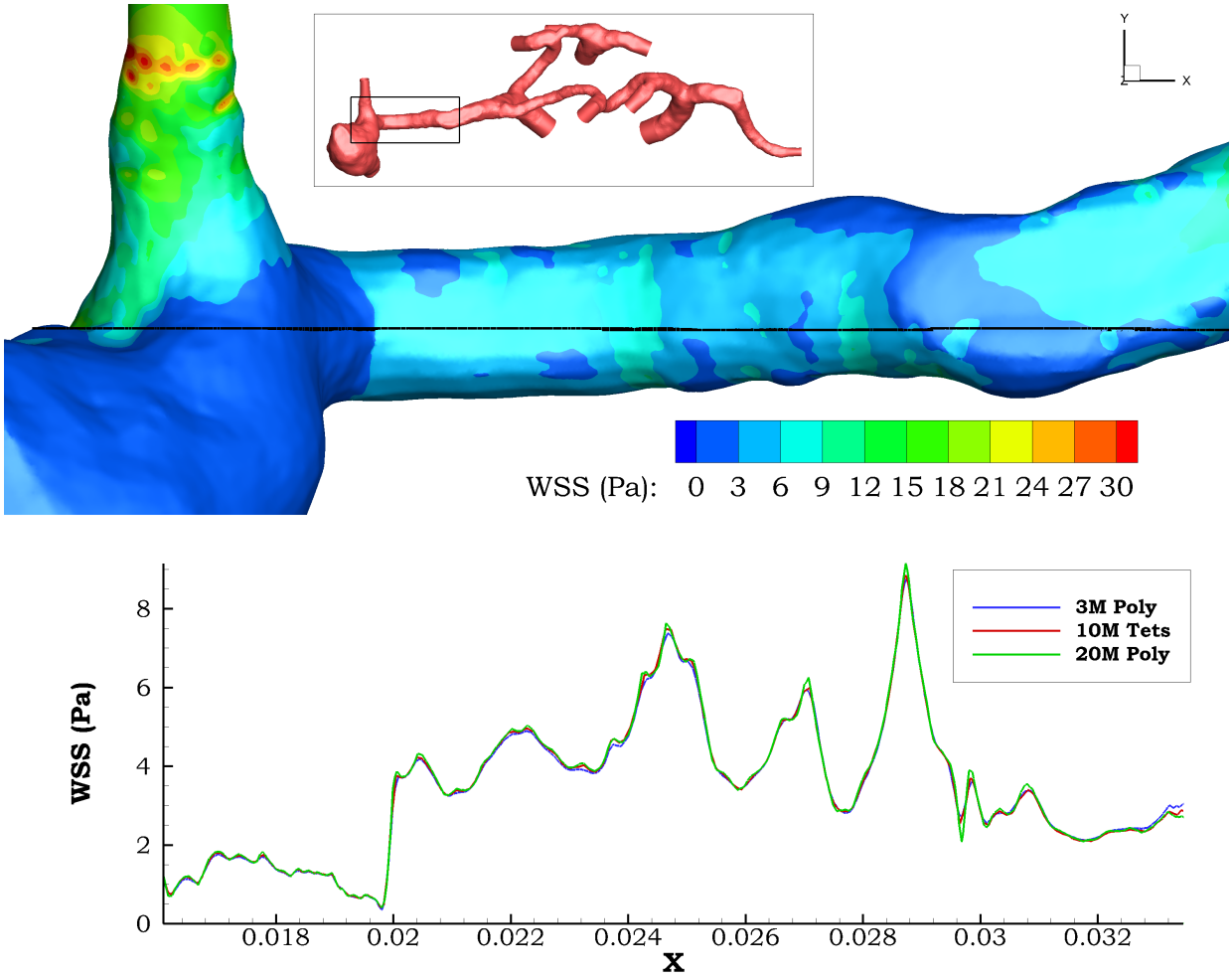

Figure 5.2: Mesh sensitivity study for the CoW geometry with aneurysm. The slice is taken at $y = 0.014$ m. The difference between the coarse polyhedral mesh, the tetrahedral mesh and the fine polyhedral mesh is less than 5 %

5.1.2. Boundary Conditions

The boundary conditions that have been used are based on the flow measurements. A parabolic inlet profile is imposed in the ICAs and BA. The boundary inflow conditions are obtained in the same way as mentioned in Section 3.2.1. The length of one heartbeat for this model is 747 ms, with the peak systole after 616 ms and the peak diastole after 356 ms. The Fourier fit for the inlet boundary conditions can be found in Figure 5.3.

For this geometry, the outflow boundary conditions are calculated with respect to the radius of the outlet artery. In Table 5.1 the mass flow fractions for the outlets are specified.

Table 5.1: Flow fractions defined for the outlets of the CoW with aneurysm geometry.

Artery	LACA	LMCA	LPCA	RACA	RMCA	RPCA	RSCA
Fraction	0.18	0.05	0.19	0.21	0.11	0.19	0.07

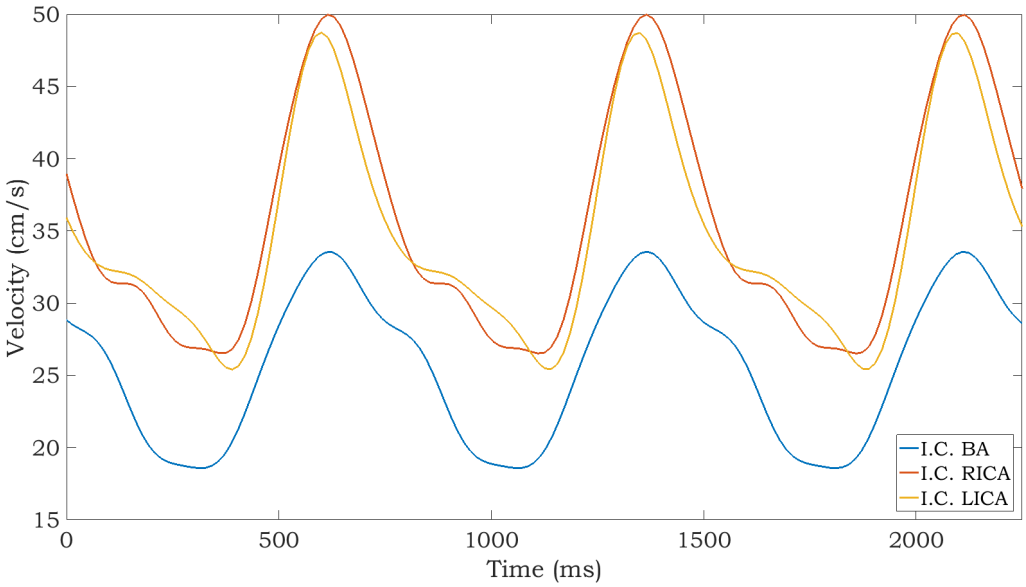

Figure 5.3: Fourier fits for the inlet boundary conditions for the CoW with aneurysm simulation

5.2. MRI vs. CFD Aneurysm

In this section, a comparison is made between MRI measurements and CFD data of the velocity inside a CoW with an aneurysm on the RMCA. In Figure 5.4 the results of this comparison are shown. It is visible that the velocity magnitude of the two plots in both the systole and the diastole is very similar. This means that the CFD simulation is capable of capturing the variations in velocity magnitude.

In the diastole, the low-velocity regions (BA, inside the aneurysm) are well-captured. In the systole, the profile is very similar as well, although there is a rise in velocity at the exit of the aneurysm, which may be due to the size of the extension inserted by VMTK.

Figure 5.5 shows a single slice taken from the MRI measurements to compare with the CFD simulations in that slice. A zoom is provided on the aneurysm itself. The figure shows some similarities in the velocity inside the aneurysm and on the other side; at the LMCA. The slices in the central part of the CoW show some differences. In the zoom image of the aneurysm, the velocity contours between MRI and CFD are very similar.

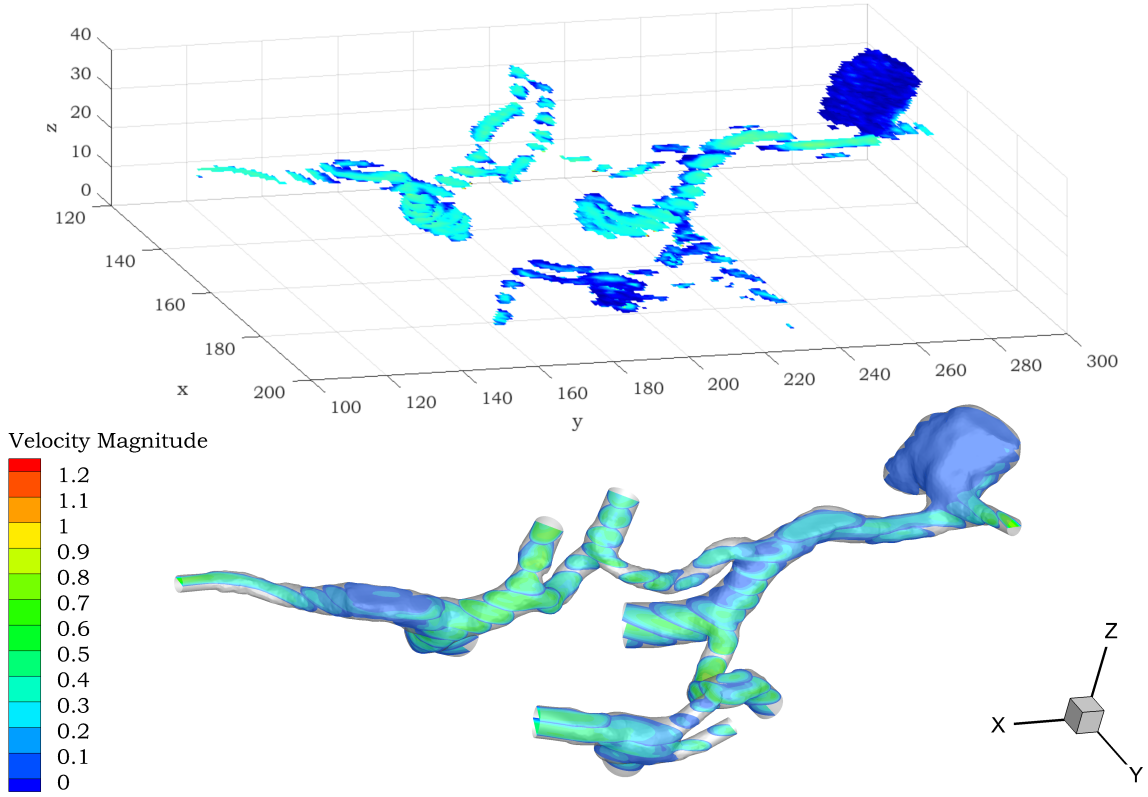

(a) Diastole

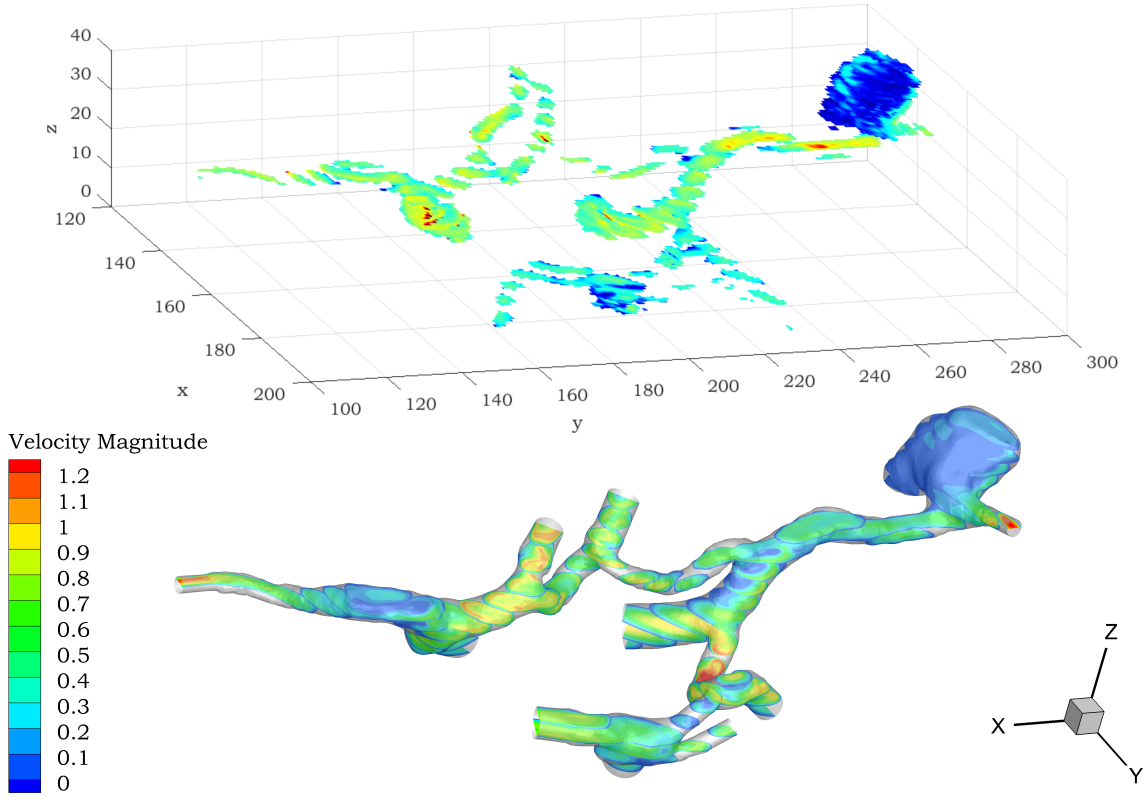

(b) Systole

Figure 5.4: The comparison of the MRI measurements (top) and CFD simulation (bottom) of the velocity magnitude in a CoW with an aneurysm for the diastole ($0.44T$) and systole ($0.77T$) phase of the cardiac cycle (0.75 s)

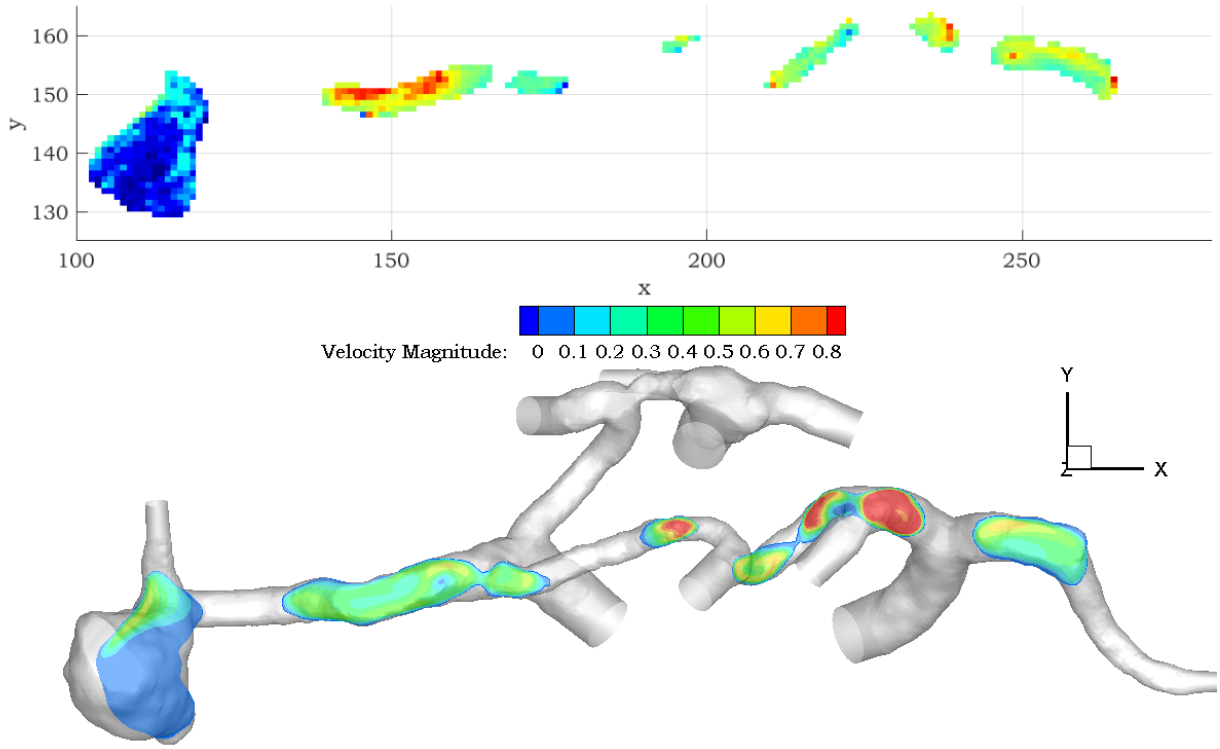

(a) Slice of CoW geometry with aneurysm comparison between MRI (top) and CFD (bottom).

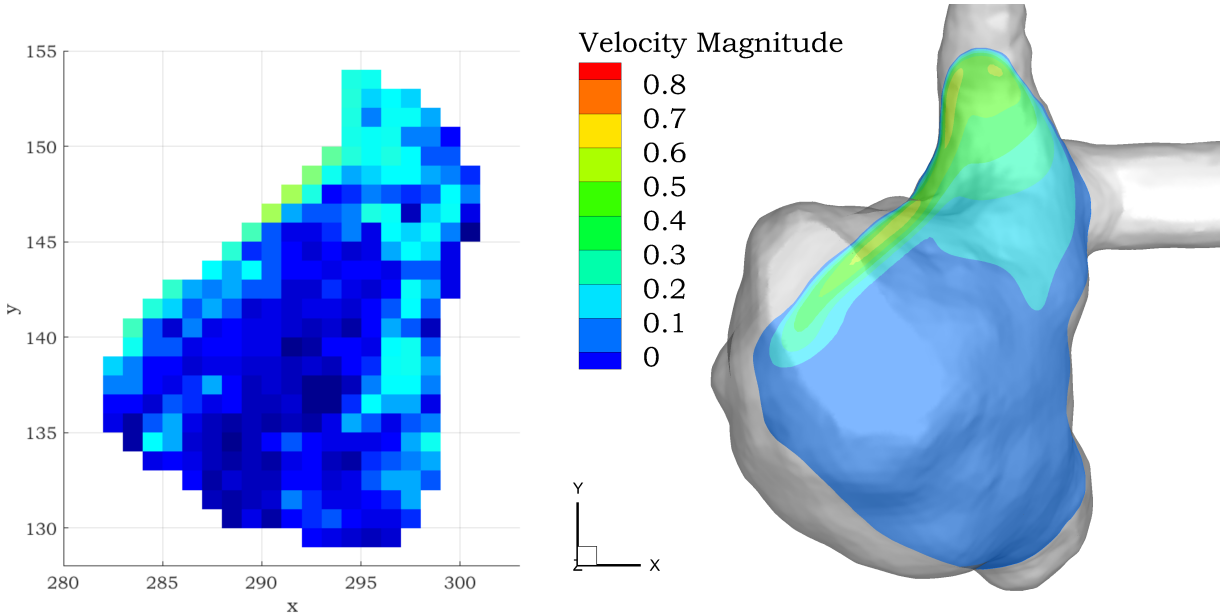

(b) Zoom of slice for the aneurysm only for MRI measurements (left) and CFD simulation (right).

Figure 5.5: The comparison of the velocity magnitude in a CoW with an aneurysm for the systole ($0.77T$) phase of the cardiac cycle (0.75 s)

5.2.1. Wall Shear Stress

The MRI measurements have also been compared to CFD simulation results based on the WSS values on the wall of the CoW. Figure 5.6 shows the relative WSS normalized by the maximum value of the MRI and CFD results, respectively. Similarities are present at the aneurysm wall, the BA surroundings, the RICA surroundings, and the RPCoA.

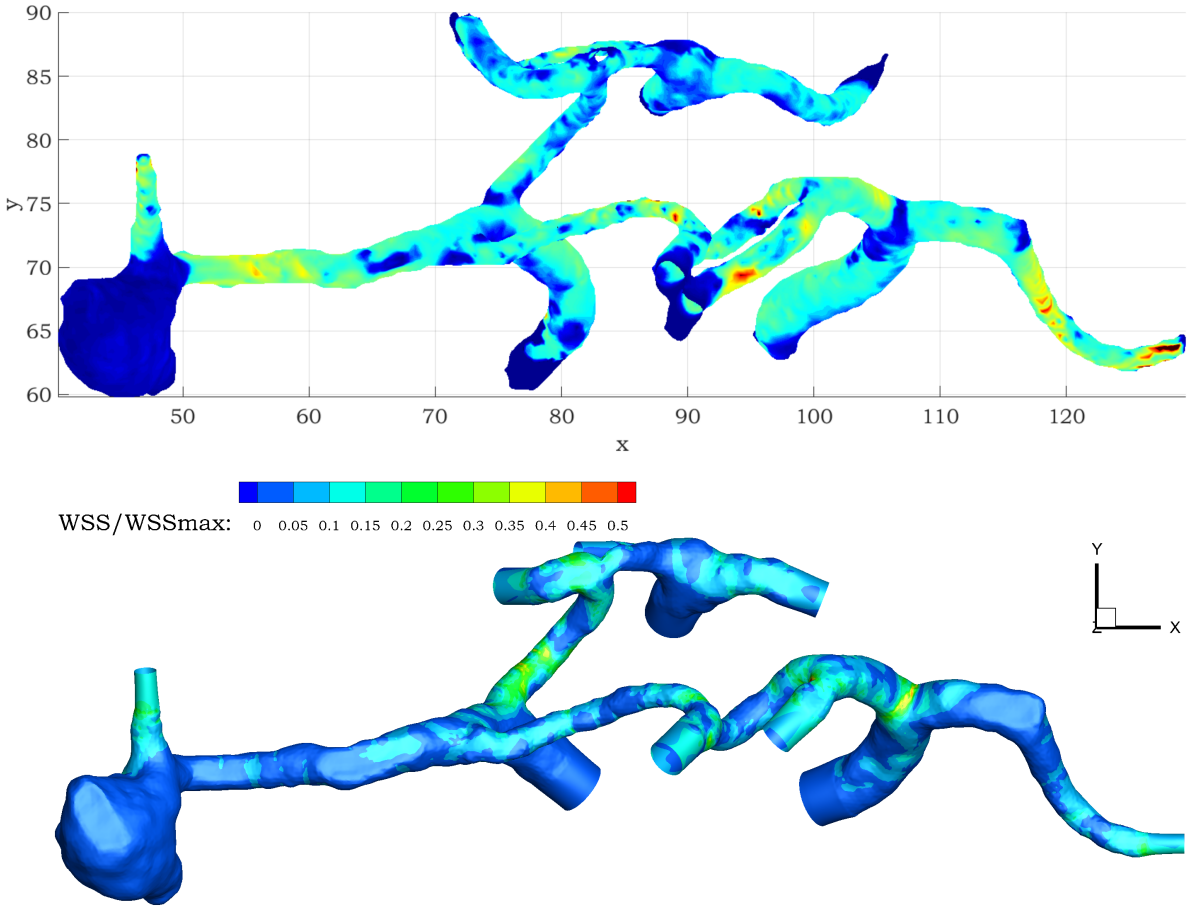

Figure 5.6: Normalized WSS values of the MRI measurements (top) and the CFD simulation results (bottom) of the CoW with aneurysm during the systole phase.

5.3. Aneurysm reduced geometry

The reduced geometry aneurysm is a section of the geometry described at the start of this Chapter.

5.3.1. Mesh

In this geometry, only the RMCA including the aneurysm is modeled. The geometry is meshed with 3 million tetrahedrals and 800k polyhedral cells. A mesh sensitivity study has been done with a finer mesh of 2.25 million cells. The difference between these simulations was less than 1 % (A.2.1).

5.3.2. Boundary Conditions

The inlet boundary conditions were obtained from MRI measurements on the RMCA. The Fourier fit for the inlet boundary conditions can be found in Figure 5.7.

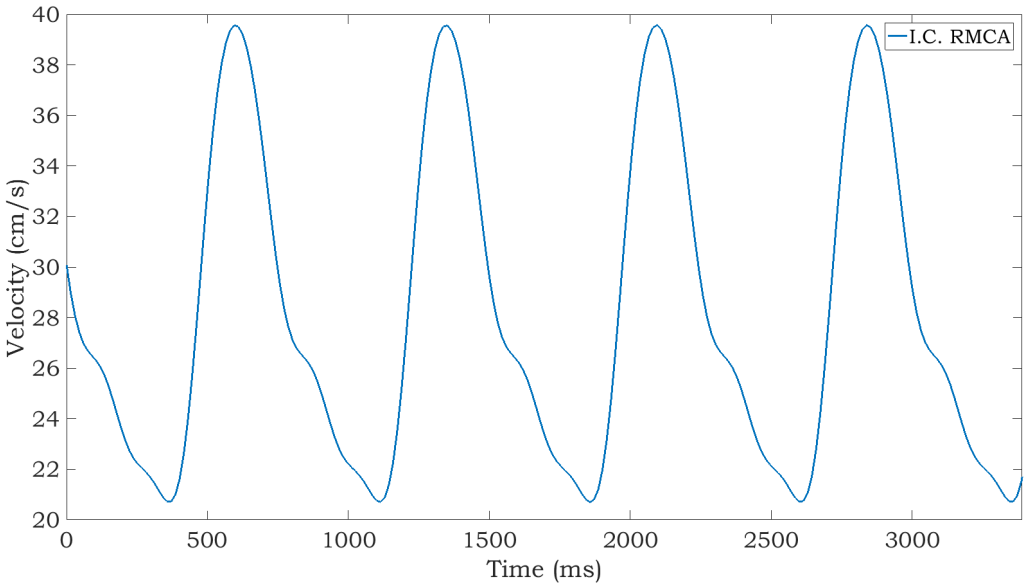

Figure 5.7: Fourier fits for the inlet boundary condition for the aneurysm and CFD challenge simulation

The velocity profile at the inlet might influence the flow profile inside the aneurysm. It is important that the inlet velocity profile is similar to the velocity profile that is simulated in the geometry with the full CoW. Figure 5.8 shows that the velocity profile in the RMCA during systole evolves from a complex profile to a profile that is close to parabolic. The profiles for the diastole look similar but have lower velocity magnitude. Therefore the simulation of the reduced geometry can be done with either parabolic of plug flow inlet velocity profiles, which will be further investigated in Section 5.4. This result contradicts the findings from Castro et al. [18], which can be explained by the long and straight shape of the RMCA in this patient-specific case.

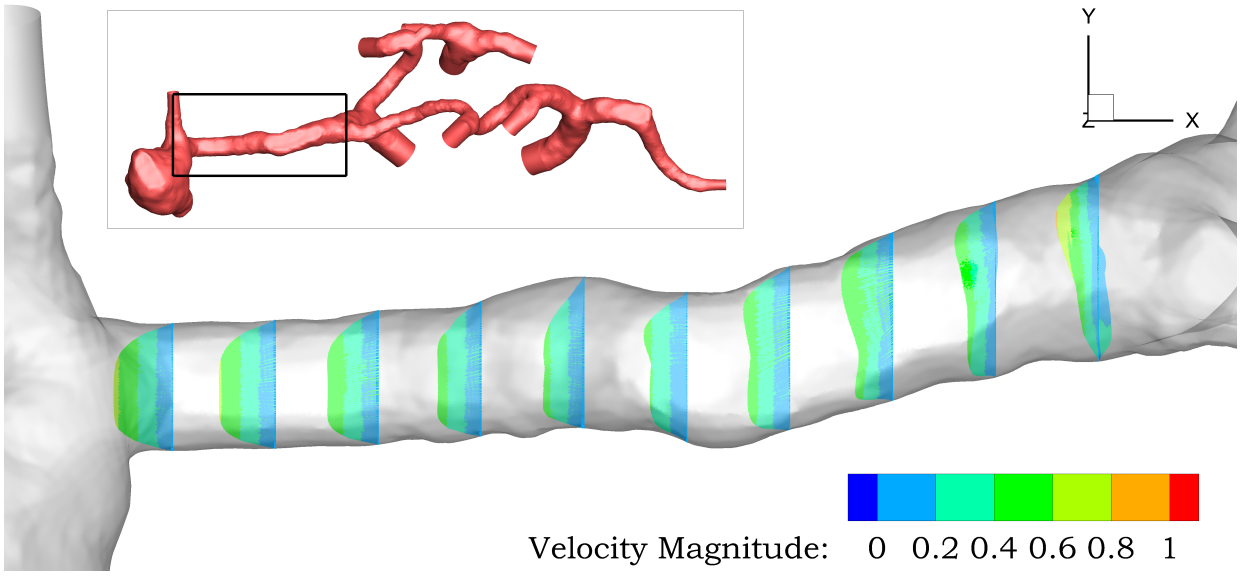

Figure 5.8: Developing velocity profiles from complex to parabolic/plug flow profile in the systole phase

5.4. Inlet flow profiles reduced geometry Aneurysm

In current literature, all aneurysm geometries are focused on the aneurysm itself, with an inlet and one or several outlets. The boundary conditions are often parabolic, uniform or Wormersley profiles that are imposed on that inlet. In this section, the shape of the velocity profile at the entrance of the aneurysm as a result of different inflow boundary conditions is compared. In the previous paragraph has been discussed that because of the length of the RMCA in the AMC aneurysm geometry, the flow entering the aneurysm is developed into a parabolic-like profile.

In Figure 5.9 the velocity profiles and the WSS values during systole in the aneurysm are compared between two cases where either a parabolic or plug flow profile was enforced at the inlet. The parabolic case and the difference between the two is shown. The velocity profiles develop inside the RMCA, where the difference between the two is the largest. When they enter the aneurysm, the difference between the flows is less than 10 %, in the aneurysm itself the difference has vanished. This result suggests that as long as the inlet artery is long enough for the flow to develop, the enforced inlet velocity profile does not matter for the flow inside the aneurysm.

The WSS values in the dome of the aneurysm are similar as well. At the inlet of the geometry differences can be found in WSS values, which can be explained by the difference in flow profiles. A plug flow profile enforces a higher velocity gradient at the wall, which causes a higher WSS value. As the plug profile develops into a more parabolic profile, the WSS values decrease and are similar to the case with a parabolic inlet flow profile. The difference of the WSS values inside the aneurysm is below 10 %.

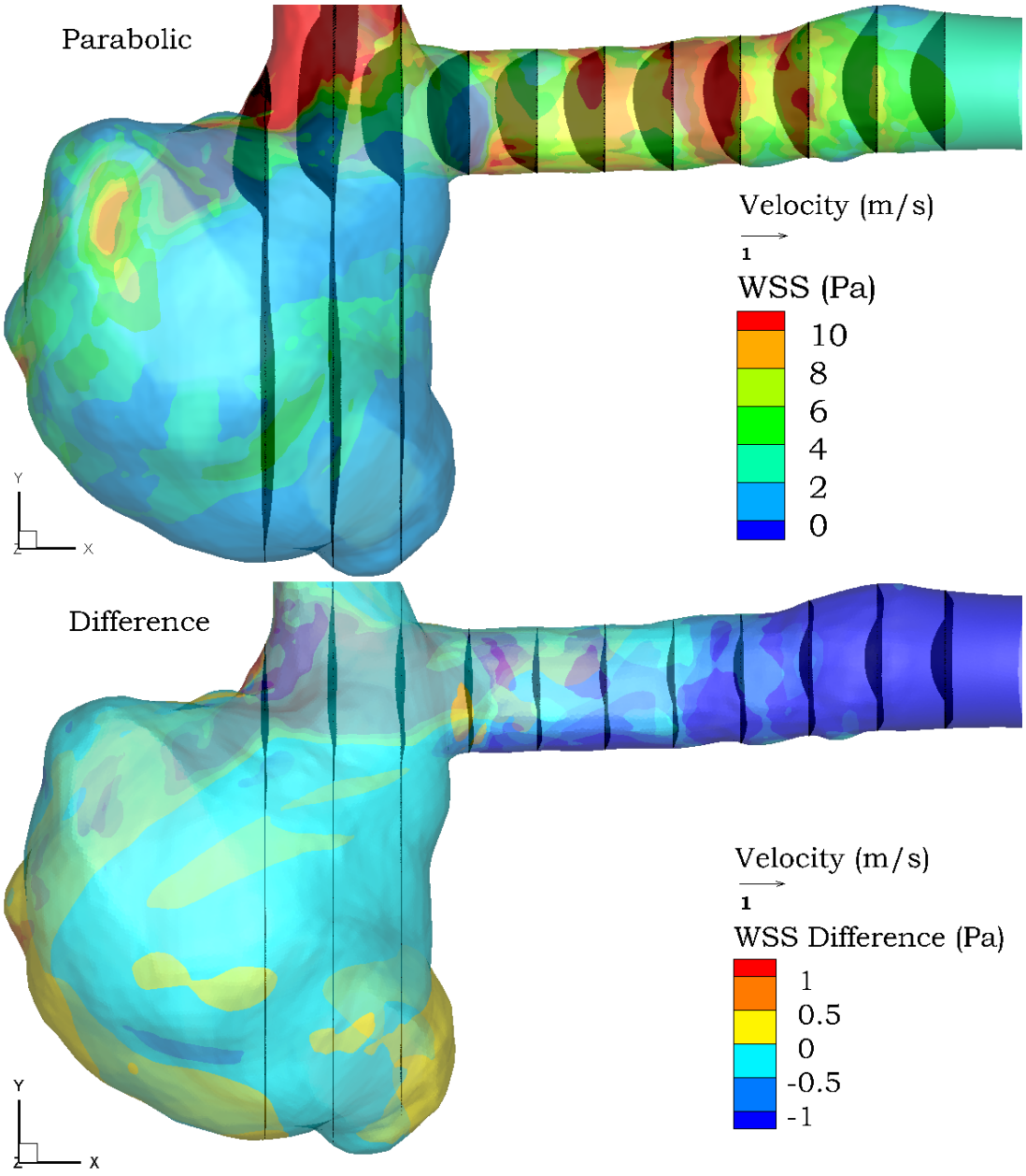

Figure 5.9: Comparison of the flow inside an aneurysm and connecting arteries between an enforced parabolic and plug velocity profile. The upper image shows the parabolic profile, the lower shows the difference between parabolic and plug in velocity vectors as well as WSS. Blood enters from the right.

5.5. Discussion

To increase understanding of aneurysms and their growth or rupture, it is important to map the hemodynamics inside the aneurysm. Previous studies that focused on aneurysms have almost always focused on the aneurysm itself, without incorporating the flow field caused by the complex geometry of the cerebral arterial system. This study compares MRI flow measurement data with CFD simulations and found a good comparison.

Additionally, the flow profile development in the artery upstream of the aneurysm has been investigated. Due to the long RMCA branch leading to the aneurysm, the flow profile was able to develop from a complex shape to a parabolic shape. This means that for this specific case it is also possible to simulate the aneurysm without the full CoW with parabolic inlet velocity conditions. This possibility will have to be assessed at each specific case.

The differences in flow structures inside the aneurysm as a result of different inlet velocity profiles were also studied. The flow structure inside the aneurysm was similar, the WSS values were similar as well.

6

Rupture Challenge

The geometry that was used in the CFD challenge of 2013 [1, 2] was simulated to test the ability of the current model to find the rupture location inside an aneurysm. In this challenge, a geometry was provided with patient-specific blood flow information, which is very similar to the boundary conditions that are imposed on the reduced aneurysm geometry. The rupture site of the aneurysm is known, so the ability of the simulation to predict the rupture site can be checked.

6.1. Methods

This geometry was meshed with 2.5 million tetrahedral cells and 600k polyhedral cells. A mesh sensitivity study has been performed with a finer mesh of 1.8 million polyhedral cells, which showed a difference in WSSTA values of 0.1 % (A.2.2).

The boundary conditions that have been used for the inlet are the same as for the AMC aneurysm model (Section 5.3.2). For the outlets a target outlet flow fraction calculated by area has been used. All other simulation settings were equal to those of the CoW Aneurysm model.

6.2. Rupture location

For both the CFD challenge Aneurysm and the aneurysm from the AMC the OSI and the WSS time-average are calculated and plotted with a Matlab routine that can be found in B.2. The locations with both a high OSI and a low WSSTA value are described as risk locations for rupture. Because no definition has been found what a 'high' or 'low' value is, the 10 % of the highest OSI values and lowest WSSTA values are intersected and a risk location map is created. In the search for a third criterion to further specify the rupture site, the 10 % of the lowest pressure values inside the aneurysm dome are intersected with the OSI and WSSTA values.

6.3. Risk of rupture

The geometry that was provided for the CFD geometry in 2013 [1, 2] was simulated make an attempt of finding the rupture site of this aneurysm. The locations with a high OSI value and

a low WSSTA value would have the highest probability to be the starting point of the rupture.

6.3.1. Criteria

The exact mathematical description of these criteria is necessary to provide a clear rupture risk map. However, in literature, no exact value is mentioned. To be able to draw conclusions, an arbitrary number of highest 10 % or lowest 10 % is chosen to make it possible to compare several criteria.

First, the cells that are inside the wall of the aneurysm are isolated. Equations (6.1) and (6.2) show how the threshold for both the OSI and the WSSTA is calculated.

$$\mathrm{OSI} > (1-G)\cdot(\mathrm{OSI}_{max}-\mathrm{OSI}_{min})+\mathrm{OSI}_{min} \tag{6.1}$$

$$\mathrm{WSSTA} < G\cdot(\mathrm{WSSTA}_{max}-\mathrm{WSSTA}_{min})+\mathrm{WSSTA}_{min} \tag{6.2}$$

where G denotes the percentage threshold. These equations calculate a percentage of the full range of either the OSI or the WSSTA, after which the threshold value is corrected by the minimum value. All cells that have OSI values above and WSSTA values below these thresholds are marked as risk locations. The percentage is varied between 1 and 25 % to illustrate the chosen threshold for both parameters. Figure 6.1 shows the areas of the aneurysm appointed as risk location colored by the percentage of the data that is taken into account. Table 6.1 shows several OSI and WSSTA values at certain percentages. For OSI these are the highest values, for WSSTA the lowest.

Criterion	**Threshold**:	**1%**	**5%**	**10%**	**15%**	**20%**	**25%**
OSI	risk above:	0.492	0.464	0.429	0.395	0.360	0.325
WSSTA (Pa)	risk below:	0.123	0.415	0.778	1.142	1.506	1.869

Table 6.1: Values of OSI and WSSTA at several threshold percentages. Higher OSI values could appoint a risk, just as lower WSSTA values. The values at 10 % are used to obtain the rupture risk plots.

In the plot for the OSI, the higher the percentages, the more risk a certain location has. That means that the highest 5 % is higher than 95 % of the calculated maximum. For the WSSTA plot, the lower percentages show a higher risk. In this aneurysm, almost all OSI values are below 75 % of the maximum, where most of the WSSTA values are within the lowest 25 % of the range. This means that when a percentage of 10 % is chosen, the WSSTA criterion will result in more 'risky' cells than the OSI criterion. The intersection of these two groups of cells will give the actual locations with a high risk of rupture. The results of this intersection is shown in Figure 6.2. This Figure shows several locations with a high risk of rupture. All sites that are highlighted have also been found by other research groups in the CFD challenge, and all sites were appointed as the rupture location at least once [2]. The correct rupture location was found by one of the groups.

Another parameter next to WSSTA and OSI might be available to further determine the rupture location. A hemodynamic evaluation was made of the vortex structures in the aneurysm dome. These are shown in red in Figure 6.3a. Streamlines were plotted around the vortex cores. Only one of the vortices bundled the streamlines that were close and created a saddle

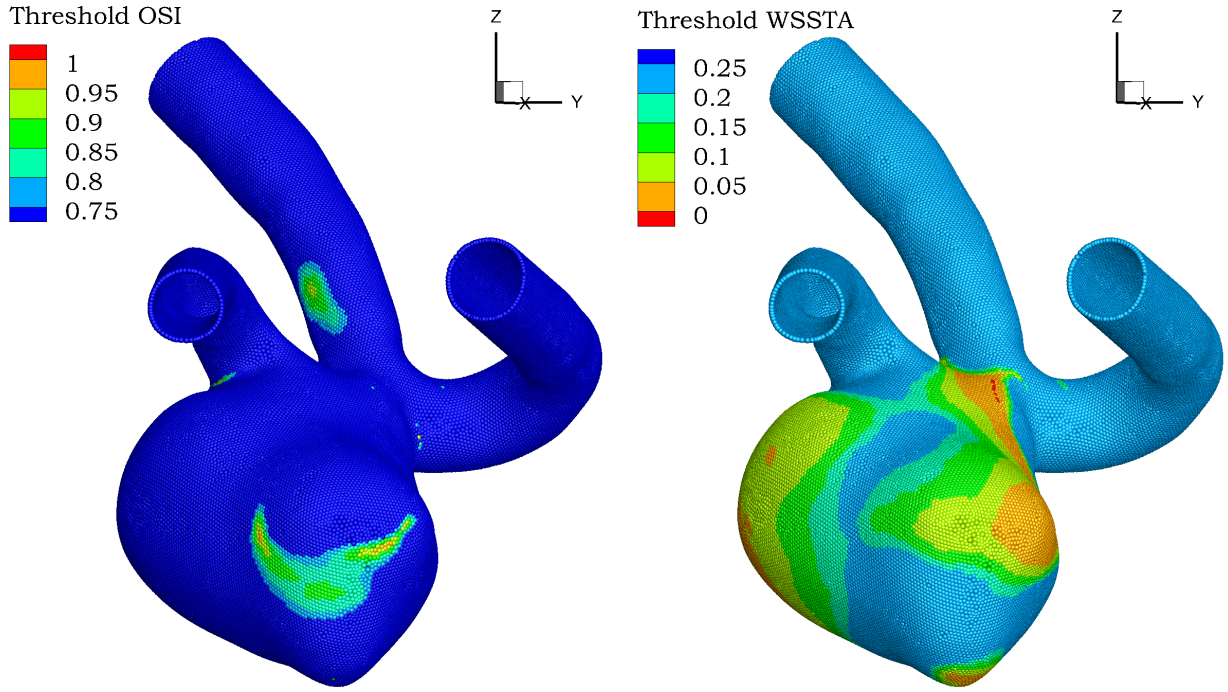

(a) OSI threshold percentages, higher values means higher rupture risk

(b) WSSTA threshold percentages, lower values means higher rupture risk

Figure 6.1: OSI and WSSTA results of the CFD challenge aneurysm.

point with the source-axis perpendicular to the wall. This vortex was located at the rupture site.

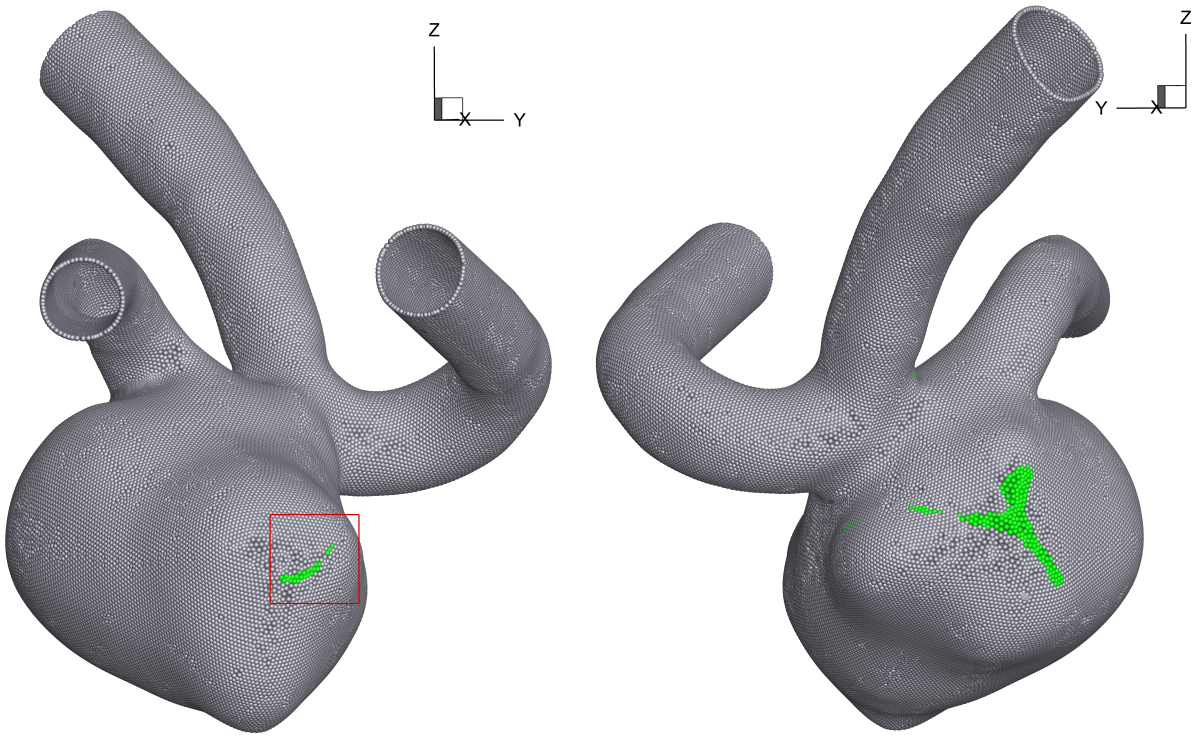

(a) Risk of rupture zones in green - front side

(b) Risk of rupture zones in green - back side

Figure 6.2: Front and back side of the aneurysm from the CFD challenge geometry. Rupture site is located inside the red square.

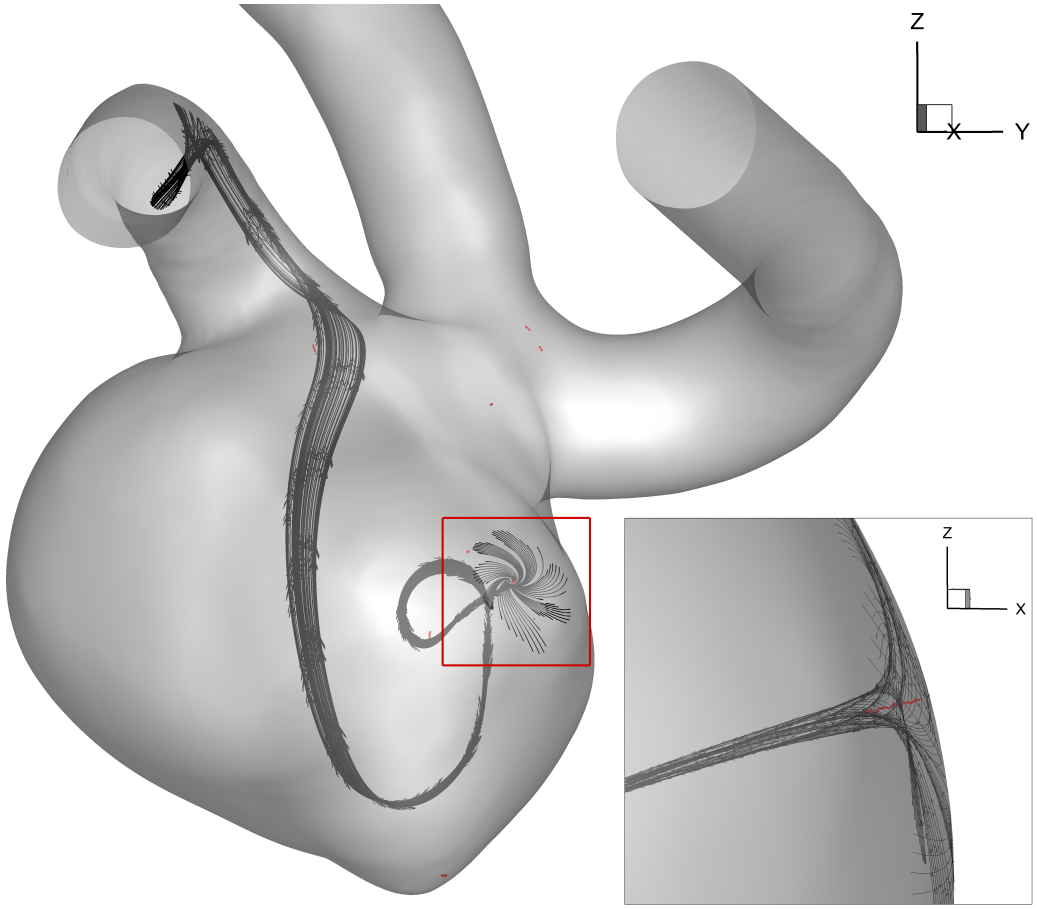

(a) The Aneurysm dome of the CFD challenge geometry with a zoom on the jet that is directed normal to the wall at the rupture site.

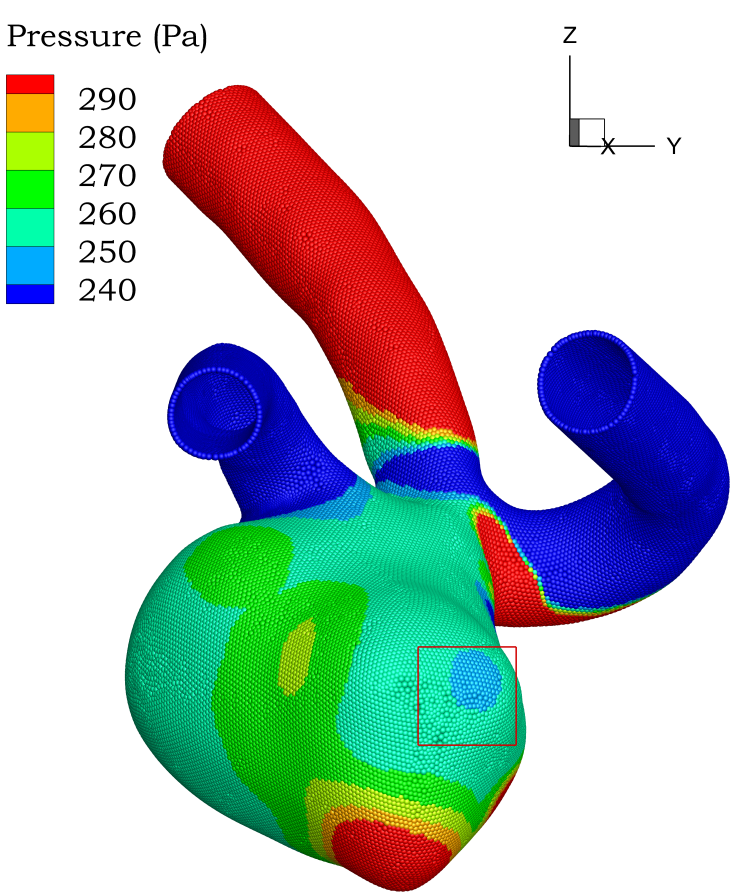

(b) The pressure distribution in the CFD challenge geometry during the systole phase of the heartbeat.

Figure 6.3: Cause of low pressure in CFD challenge aneurysm.

As a result of this saddle point in the flow, it is expected that during the systole phase, the pressure is lower on this part of the wall. This phenomenon is not present during diastole. This means that on this part of the wall not only the OSI is high, but the normal stress does also oscillate. This could mean that the aneurysm wall at that point vibrates as a result of these pressure differences. This could eventually lead to rupture due to fatigue of the wall tissue [50]. Therefore an extra criterion was added that shows the location with the 10 % lowest pressure values. The way this phenomenon is calculated is given by (6.3).

$$P_{wall} \quad > \quad G \cdot (P_{wall,max} - P_{wall,min}) + P_{wall,min} \tag{6.3}$$

Implementing this criterion leads to a rupture risk location image that is shown in Figure 6.4. Only one location with a high rupture risk is present when pressure is included in the risk analysis. That location is the actual rupture location.

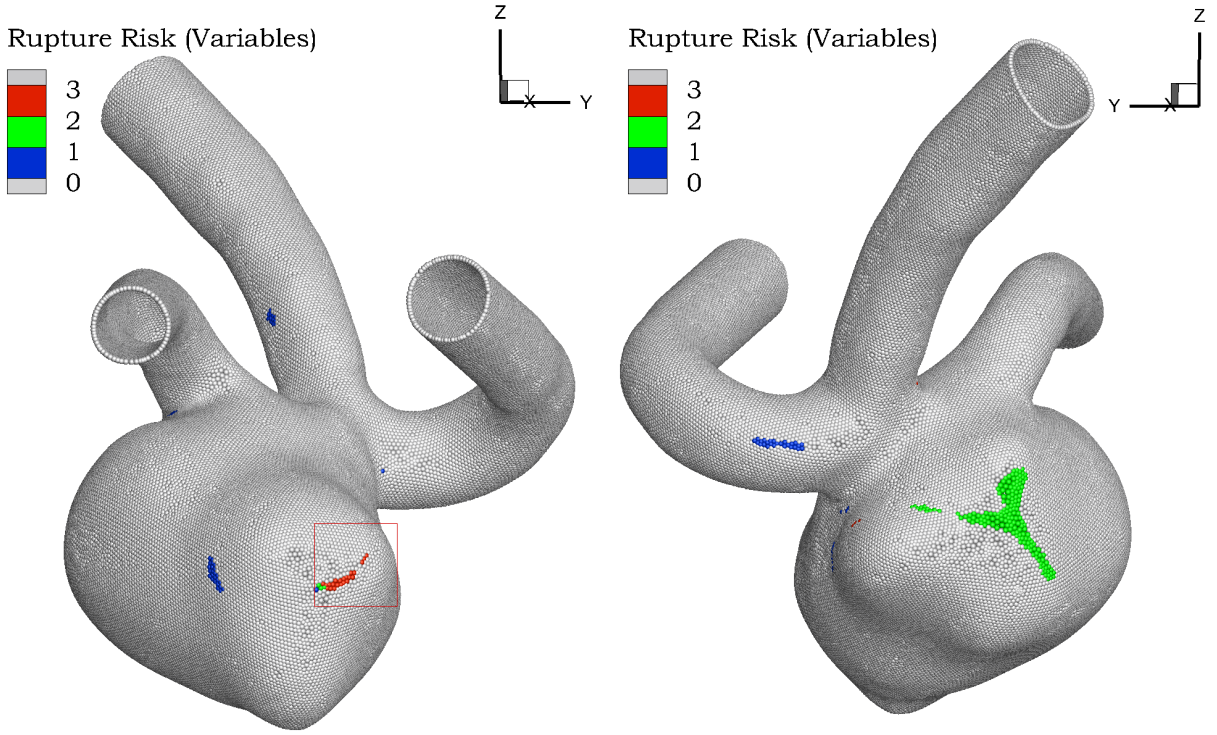

(a) Front view (b) Back view

Figure 6.4: Front and back side of the aneurysm from the CFD challenge geometry with the rupture risk locations derived from two and three criteria. Rupture site is located inside the red square.

6.4. Reduced geometry aneurysm

The same rupture risk analysis has been done on the reduced geometry of the aneurysm obtained from the AMC. The risk evaluation on one (OSI), two (OSI and WSSTA), and three criteria is shown in Figure 6.5. Only one site is appointed as the possible rupture site by the combination of the three criteria.

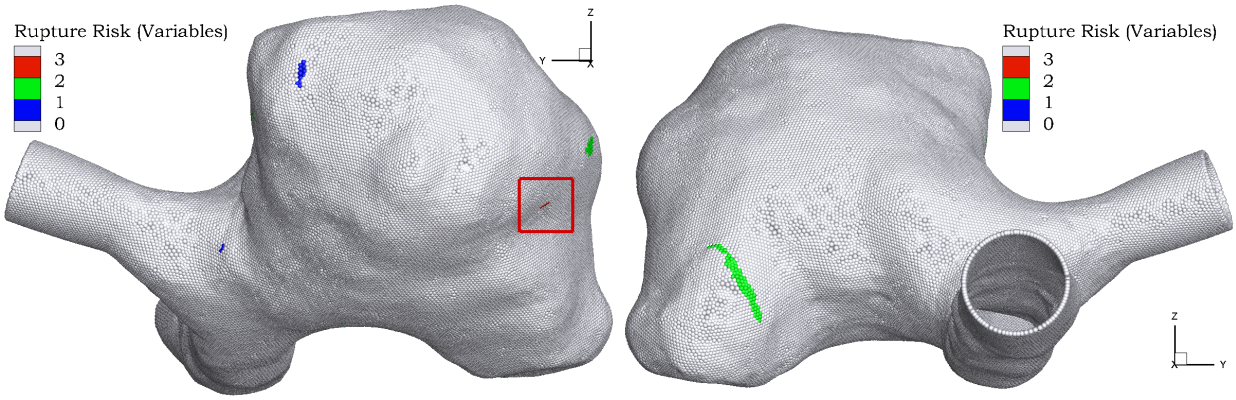

Figure 6.5: Rupture risk locations at the aneurysm from the AMC. In blue, the locations with a high OSI value are shown, in green, the locations with a high OSI and low WSSTA value are shown, red shows the addition of the pressure criterion.

The hemodynamic analysis has also been done on this geometry. Figure 6.6 shows the same vortex structure as shown in the previous section. The location of this vortex structure coincides with the proposed rupture risk location from Figure 6.5. None of the other vortex cores show this behavior. The vortex structure causes a relatively low-pressure region in this geometry as well, so that the use of pressure as a third criterion is justified.

6.5. Discussion

It is still a challenge to find a reliable criterion to assess the danger of an unruptured aneurysm. Instead of depending the need for surgery on the size of the aneurysms, hemodynamic criteria are investigated to study the risk of rupture. However, these two criteria that have been used until now, OSI and WSSTA, do not always give the correct location of rupture. This seems to coincide with the lack of links between the hemodynamic and biomechanic properties at the aneurysm wall. In the present study, a third criterion is proposed to be added to the two existing criteria. A vortex structure with a saddle point is found, with a resulting lower pressure region at the wall. With this third criterion, the location of rupture of an aneurysm can be predicted more accurately. It should be noted that the present hypothesis is based on two numerical case studies. Of course, the hypothesis should be tested in a number of different cases. Nevertheless, the hypothesis is appealing since it combines factors that are aligned with a plausible failure mechanism of the aneurysm wall.

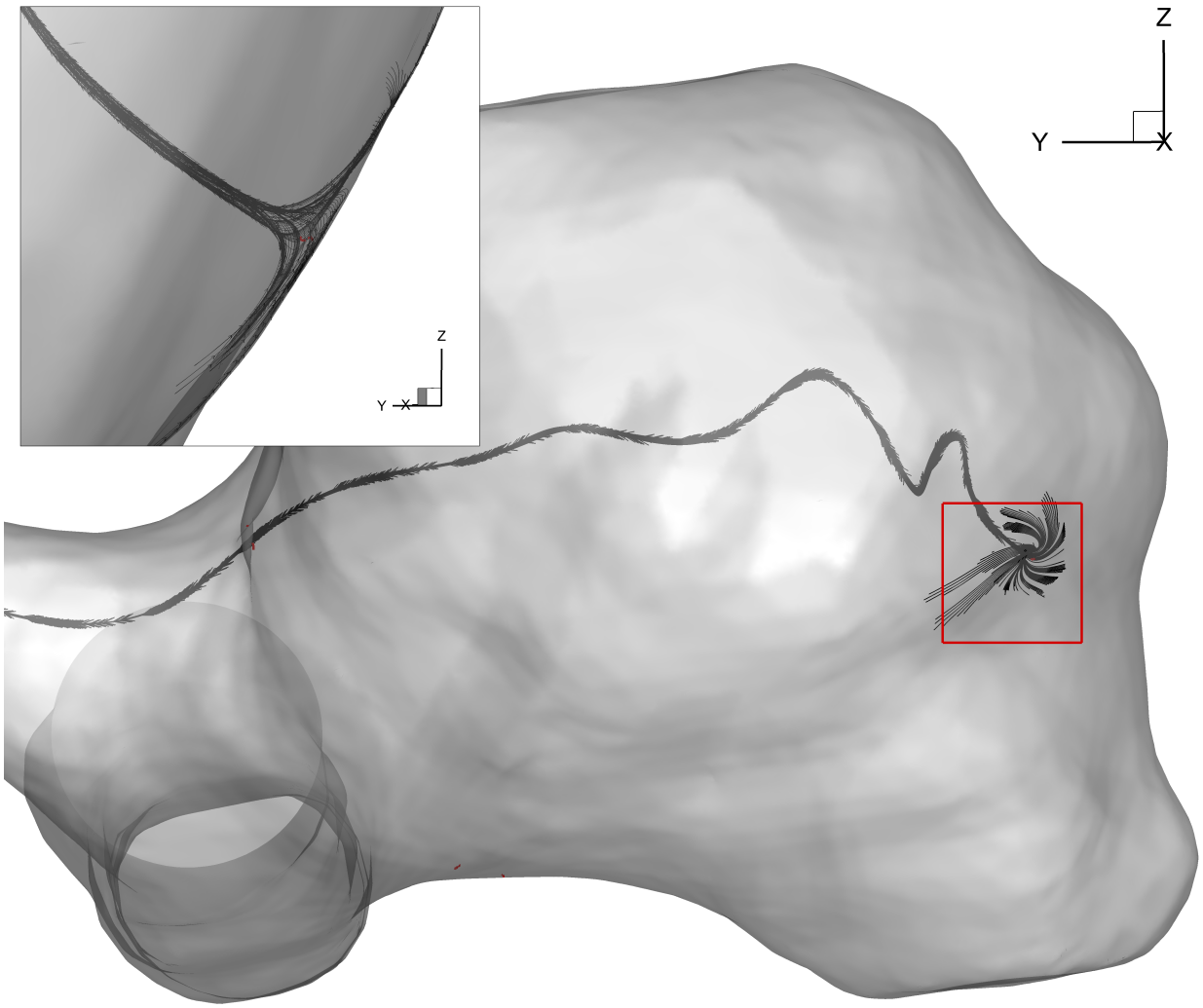

Figure 6.6: The aneurysm dome of the reduced geometry geometry with a zoom on the jet that is directed normal to the wall at the rupture site.

7

Concluding remarks

In this research, CFD simulations for a healthy Circle of Willis (CoW) have been done to validate the simulation model with MRI data. These validated models have been applied to a CoW with an aneurysm to investigate the hemodynamics inside of an aneurysm. Additionally, a simulation has been done on the geometry from the CFD challenge 2013 (Janiga et al. [1], Berg et al. [2]), to find the rupture site inside an aneurysm and to evaluate the parameters that are used to find that rupture site. These analyses have been performed on the AMC aneurysm as well. From these studies, the following concluding remarks can be made.

The following research questions were formulated and their answers are given:

- *Can a CFD simulation be used to mimic MRI velocity measurement data, and to what extent is this possible?*
  The CFD model in the present study has successfully been used to mimic the MRI data obtained for a patient-specific geometry of a healthy Circle of Willis.
  Velocity values are in good agreement with the MRI data provided. This conclusion is in agreement with the conclusions drawn by Perinajová [13]. For the WSS, the agreement is good in terms of flow characteristics, both methods show similarities. The differences can be attributed to the limited resolution of the MRI data, in comparison to CFD, that shows up in the calculation of the WSS values in the MRI data due to gradients in the velocity data.

- *What effect do blood thinners have on velocity profiles and WSS values?*
  When blood thinners are present in the blood, this has a slight lowering effect on the WSS values inside the CoW.
  Due to the lower WSS the muscular fibers in the blood vessels are enforced to contract more, due to a decreased release of NO. This might lead to wear of these muscles, and thus enlarge the risk of aneurysms. This might be an interesting topic for research of a more medical nature. Next to that lower WSS(TA) values is one of the criteria that have a positive influence on the growth of aneurysms and their rupture [1, 2].

- *What effect do inlet velocity profiles have on flow structure and WSS values in aneurysms?*
  The difference between a plug flow profile and a parabolic profile is negligible, as long as the inlet is long enough for the flow to develop.
  The inlet artery that leads towards the aneurysm causes the flow velocity profile to de-

velop further, such that no difference can be seen between the profiles at the neck of the aneurysm. The WSS values are similar in both cases as well. This conclusion agrees with Berg and Beuing [24], who state that modeling the aneurysm without the full vasculature still gives good agreement.

- *Which parameters next to the Oscillatory Shear Index (OSI) and Wall Shear Stress Time-Average (WSSTA) can be found as criteria for aneurysm rupture?*
  Next to OSI and WSSTA, which could be successfully extracted and visualized, vortex structures at the wall in the systole phase that cause the flow to form a jet off the wall in the normal direction could be another criterion to predict aneurysm rupture. This phenomenon can be measured as a drop in pressure at the wall at the location of the vortex structure.
  With the OSI, WSSTA and pressure criteria combined, the correct location of the rupture inside an aneurysm has been found. This means that the jet-like flow, that is produced by the vortex during the systole phase, causes a pressure drop on the aneurysm wall in such a way that a weakened part of the wall might rupture.

From the answers to these sub-questions the main research question can be answered. A CFD model can be used to assess the hemodynamics in intracranial aneurysms and for two aneurysm geometries it is possible to predict the possible rupture site in an aneurysm with this model.

8

Recommendations

In this Chapter, several recommendations will be made for further research.

- Research on the influence of blood thinners on the formation of aneurysms. Statistical data could be used to confirm that blood-thinners have an enlarging effect on the risk of genesis and rupture of aneurysms.
- Further analyze whether a full CoW model is necessary to successfully simulate the flow structure inside aneurysms:
  - By including Wormersley flow as an inlet boundary condition in the reduced geometry of aneurysm.
  - By extracting the velocity profile from the CoW simulation and implementing that as an inlet boundary condition of the reduced geometry.
- Creating a UDF to visualize OSI and WSSTA results within CFD post-processing routines. This could streamline the evaluation process of the simulations.
- Evaluate more aneurysms with known rupture sites to test the hypothesis that vortex structures in combination with low pressure values are another criterion to predict the rupture of aneurysms.
- Combine hemodynamic properties inside the aneurysm with mechanical information about the aneurysm wall to investigate the both influences on aneurysm rupture. From this an absolute criterion can be distilled for the parameters involved in aneurysm rupture.
- Perform in-vitro experiments on a model of a CoW with an aneurysm to validate the CFD simulations done in this study.

Bibliography

[1] G. Janiga, P. Berg, S. Sugiyama, K. Kono, and D. Steinman. The Computational Fluid Dynamics rupture challenge 2013—phase i: prediction of rupture status in intracranial aneurysms. *American Journal of Neuroradiology*, 36(3):530–536, 2015.

[2] P. Berg, C. Roloff, O. Beuing, S. Voss, S.-I. Sugiyama, N. Aristokleous, A. S. Anayiotos, N. Ashton, A. Revell, N. W. Bressloff, et al. The Computational Fluid Dynamics rupture challenge 2013—phase ii: variability of hemodynamic simulations in two intracranial aneurysms. *Journal of Biomechanical Engineering*, 137(12):121008, 2015.

[3] Brain-Aneurysm-Foundation. Brain Aneurysm Statistics and Facts. Visited on 13-09-2017, 2017. URL https://www.bafound.org/about-brain-aneurysms/brain-aneurysm-basics/brain-aneurysm-statistics-and-facts/.

[4] M. K. Abraham and W.-T. W. Chang. Subarachnoid hemorrhage. *Emergency Medicine Clinics*, 34(4):901–916, 2016.

[5] B. Wedro. Brain Aneurysm (Cerebral Aneurysm). Visited on 13-09-2017, 2017. URL http://www.medicinenet.com/brain_aneurysm/article.htm.

[6] R. J. Komotar, J. Mocco, and R. A. Solomon. Guidelines for the surgical treatment of unruptured intracranial aneurysms: the first annual J. Lawrence pool memorial research symposium—controversies in the management of cerebral aneurysms. *Neurosurgery*, 62 (1):183–194, 2008.

[7] M. L. Raghavan, B. Ma, and R. E. Harbaugh. Quantified aneurysm shape and rupture risk. *Journal of Neurosurgery*, 102(2):355–362, 2005.

[8] M. Markl, W. Wallis, and A. Harloff. Reproducibility of flow and Wall Shear Stress analysis using flow-sensitive four-dimensional MRI. *Journal of Magnetic Resonance Imaging*, 33 (4):988–994, 2011.

[9] J. R. Cebral, C. M. Putman, M. T. Alley, T. Hope, R. Bammer, and F. Calamante. Hemodynamics in normal cerebral arteries: qualitative comparison of 4D phase-contrast magnetic resonance and image-based Computational Fluid Dynamics. *Journal of Engineering Mathematics*, 64(4):367, 2009.

[10] S. Meier, A. Hennemuth, O. Friman, J. Bock, M. Markl, and T. Preusser. Non-invasive 4D blood flow and pressure quantification in central blood vessels via PC-MRI. In *Computing in Cardiology, 2010*, pages 903–906. IEEE, 2010.

[11] V. C. Rispoli, J. F. Nielsen, K. S. Nayak, and J. L. Carvalho. Computational Fluid Dynamics simulations of blood flow regularized by 3D phase contrast MRI. *Biomedical Engineering online*, 14(1):110, 2015.

[12] H. Gharahi, B. A. Zambrano, D. C. Zhu, J. K. DeMarco, and S. Baek. Computational Fluid Dynamic simulation of human carotid artery bifurcation based on anatomy and volu-

metric blood flow rate measured with Magnetic Resonance Imaging. *International Journal of advances in Engineering Sciences and Applied Mathematics*, 8(1):46–60, 2016.

[13] R. Perinajová. Numerical simulations of blood flow and oxygen mass transfer in a patient specific cerebrovascular system, 2017.

[14] D. I. Hollnagel, P. E. Summers, D. Poulikakos, and S. S. Kollias. Comparative velocity investigations in cerebral arteries and aneurysms: 3D phase-contrast MR angiography, laser Doppler velocimetry and Computational Fluid Dynamics. *NMR in Biomedicine*, 22(8): 795–808, 2009.

[15] H. Isoda, Y. Ohkura, T. Kosugi, M. Hirano, M. T. Alley, R. Bammer, N. J. Pelc, H. Namba, and H. Sakahara. Comparison of hemodynamics of intracranial aneurysms between MR fluid dynamics using 3D cine phase-contrast MRI and MR-based Computational Fluid Dynamics. *Neuroradiology*, 52(10):913–920, 2010.

[16] P. van Ooij, A. Guédon, C. Poelma, J. Schneiders, M. Rutten, H. Marquering, C. Majoie, E. VanBavel, and A. Nederveen. Complex flow patterns in a real-size intracranial aneurysm phantom: phase contrast MRI compared with particle image velocimetry and Computational Fluid Dynamics. *NMR in Biomedicine*, 25(1):14–26, 2012.

[17] P. Berg, D. Stucht, G. Janiga, O. Beuing, O. Speck, and D. Thévenin. Cerebral blood flow in a healthy Circle of Willis and two intracranial aneurysms: Computational Fluid Dynamics versus four-dimensional phase-contrast Magnetic Resonance Imaging. *Journal of Biomechanical Engineering*, 136(4):041003, 2014.

[18] M. Castro, C. Putman, and J. Cebral. Computational Fluid Dynamics modeling of intracranial aneurysms: effects of parent artery segmentation on intra-aneurysmal hemodynamics. *American Journal of Neuroradiology*, 27(8):1703–1709, 2006.

[19] J. R. Cebral, M. A. Castro, J. E. Burgess, R. S. Pergolizzi, M. J. Sheridan, and C. M. Putman. Characterization of cerebral aneurysms for assessing risk of rupture by using patient-specific computational hemodynamics models. *American Journal of Neuroradiology*, 26 (10):2550–2559, 2005.

[20] S. Tateshima, K. Tanishita, and F. Vinuela. Hemodynamics and cerebrovascular disease. *World Neurosurgery*, 70(5):447–453, 2008.

[21] D. M. Sforza, C. M. Putman, and J. R. Cebral. Computational Fluid Dynamics in brain aneurysms. *International Journal for numerical methods in Biomedical Engineering*, 28 (6-7):801–808, 2012.

[22] A. Robertson and P. Watton. Computational Fluid Dynamics in aneurysm research: critical reflections, future directions, 2012.

[23] S. S. Shishir, M. A. K. Miah, A. S. Islam, and A. T. Hasan. Blood flow dynamics in cerebral aneurysm-a CFD simulation. *Procedia Engineering*, 105:919–927, 2015.

[24] P. Berg and O. Beuing. Multiple intracranial aneurysms: a direct hemodynamic comparison between ruptured and unruptured vessel malformations. *International Journal of Computer Assisted Radiology and Surgery*, 13(1):83–93, 2018.

[25] N. Varble, G. Trylesinski, J. Xiang, K. Snyder, and H. Meng. Identification of vortex struc-

tures in a cohort of 204 intracranial aneurysms. *Journal of The Royal Society Interface*, 14 (130):20170021, 2017.

[26] D. N. Ku, D. P. Giddens, C. K. Zarins, and S. Glagov. Pulsatile flow and atherosclerosis in the human carotid bifurcation. positive correlation between plaque location and low oscillating shear stress. *Arteriosclerosis, Thrombosis, and Vascular Biology*, 5(3):293–302, 1985.

[27] J. Xiang, S. K. Natarajan, M. Tremmel, D. Ma, J. Mocco, L. N. Hopkins, A. H. Siddiqui, E. I. Levy, and H. Meng. Hemodynamic–morphologic discriminants for intracranial aneurysm rupture. *Stroke*, 42(1):144–152, 2011.

[28] Y. Miura, F. Ishida, Y. Umeda, H. Tanemura, H. Suzuki, S. Matsushima, S. Shimosaka, and W. Taki. Low wall shear stress is independently associated with the rupture status of middle cerebral artery aneurysms. *Stroke*, 44(2):519–521, 2013.

[29] P. Berg, G. Janiga, O. Beuing, M. Neugebauer, and D. Thévenin. Hemodynamics in multiple intracranial aneurysms: The role of shear related to rupture. *International Journal of Bioscience, Biochemistry and Bioinformatics*, 3(3):177, 2013.

[30] H. Meng, V. Tutino, J. Xiang, and A. Siddiqui. High WSS or low WSS? Complex interactions of hemodynamics with intracranial aneurysm initiation, growth, and rupture: toward a unifying hypothesis. *American Journal of Neuroradiology*, 35(7):1254–1262, 2014.

[31] N. V. Kulkarni. *Clinical Anatomy (a problem solving approach)*. JP Medical Ltd, 2011.

[32] I. D. Šutalo, A. V. Bui, S. Ahmed, K. Liffman, and R. Manasseh. Modeling of flow through the circle of willis and cerebral vasculature to assess the effects of changes in the peripheral small cerebral vasculature on the inflows. *Engineering Applications of Computational Fluid Mechanics*, 8(4):609–622, 2014.

[33] SEER-Training-Modules. Classification and Structure of Blood Vessels. Visited on 30-01-2018, 2017. URL https://training.seer.cancer.gov/anatomy/cardiovascular/blood/classification.html.

[34] A. Sandoo, J. J. V. van Zanten, G. S. Metsios, D. Carroll, and G. D. Kitas. The endothelium and its role in regulating vascular tone. *The open cardiovascular medicine Journal*, 4:302, 2010.

[35] A. Dusak, K. Kamasak, C. Goya, M. E. Adin, M. A. Elbey, and A. Bilici. Arterial distensibility in patients with ruptured and unruptured intracranial aneurysms: is it a predisposing factor for rupture risk? *Medical science monitor: international medical Journal of experimental and clinical research*, 19:703, 2013.

[36] A. Selimovic, Y. Ventikos, and P. N. Watton. Modelling the evolution of cerebral aneurysms: Biomechanics, mechanobiology and multiscale modelling. *Procedia IUTAM*, 10:396–409, 2014.

[37] A. S. Fauci et al. *Harrison's principles of Internal Medicine*, volume 2. McGraw-Hill, Medical Publishing Division New York, 2008.

[38] C. Sadasivan, D. J. Fiorella, H. H. Woo, and B. B. Lieber. Physical factors effecting cerebral aneurysm pathophysiology. *Annals of Biomedical Engineering*, 41(7):1347–1365, 2013.

[39] C. R. White, H. Y. Stevens, M. Haidekker, and J. A. Frangos. Temporal gradients in shear, but not spatial gradients, stimulate ERK1/2 activation in human endothelial cells. *American Journal of Physiology-Heart and Circulatory Physiology*, 289(6):H2350–H2355, 2005.

[40] T. B. Le, I. Borazjani, and F. Sotiropoulos. Pulsatile flow effects on the hemodynamics of intracranial aneurysms. *Journal of Biomechanical Engineering*, 132(11):111009, 2010.

[41] L. Goubergrits, J. Schaller, U. Kertzscher, N. van den Bruck, K. Pöthkow, C. Petz, H.-C. Hege, and A. Spuler. Statistical Wall Shear Stress maps of ruptured and unruptured middle cerebral artery aneurysms. *Journal of the Royal Society Interface*, 9(69):677–688, 2012.

[42] M. Hitosugi, M. Niwa, and A. Takatsu. Changes in blood viscosity by heparin and argatroban. *Thrombosis research*, 104(5):371–374, 2001.

[43] J. R. Womersley. An elastic tube theory of pulse transmission and oscillatory flow in mammalian arteries. Technical report, AEROSPACE RESEARCH LABS WRIGHT-PATTERSON AFB OH, 1957.

[44] D. N. Ku. Blood flow in arteries. *Annual Review of Fluid Mechanics*, 29(1):399–434, 1997.

[45] Fluent and ANSYS. 17.0, Theory Guide; ANSYS. *Inc., Canonsburg, PA*, 2015.

[46] M. Khan, K. Valen-Sendstad, and D. Steinman. Narrowing the expertise gap for predicting intracranial aneurysm hemodynamics: impact of solver numerics versus mesh and time-step resolution. *American Journal of Neuroradiology*, 36(7):1310–1316, 2015.

[47] K. Hanjalić, S. Kenjereš, M. Tummers, and H. Jonker. *Analysis and modelling of physical transport phenomena*. VSSD, 2007.

[48] T. F. Sherman. On connecting large vessels to small. The meaning of Murray's law. *The Journal of General Physiology*, 78(4):431–453, 1981.

[49] S. Manini and L. Antiga. VMTK documentation. Visited on 10-10-2017, 2017. URL http://www.vmtk.org/what-is-vmtk.html.

[50] P. Mitchell, D. Birchall, and A. D. Mendelow. Blood pressure, fatigue, and the pathogenesis of aneurysmal subarachnoid hemorrhage. *Surgical neurology*, 66(6):574–580, 2006.

A

Results

In this part of the appendix a selection of results images can be found that have been left out of the main text.

A.1. CoW vs. MRI

Table A.1 shows the flow through several slices of the RMCA, measured by the 7T MRI scanner from the AMC. The flow deviates up to 30 % from the median.

$t = 0.000$ s		$t = 0.658$ s		$t = 0.940$ s	
Flow (ml/s)	Deviation from median (%)	Flow (ml/s)	Deviation from median (%)	Flow (ml/s)	Deviation from median (%)
1.95	7.43	1.34	32.11	2.23	1.38
1.96	8.06	1.05	3.04	2.09	-4.88
1.71	-5.69	1.02	0.29	2.03	-7.54
1.82	0.60	0.93	-8.33	2.05	-6.97
1.68	-7.50	0.93	-8.79	1.98	-9.77
1.74	-4.23	0.96	-5.46	2.17	-1.38
1.89	4.50	1.00	-1.19	2.86	30.19
1.76	-2.97	1.14	12.32	2.61	18.71
1.80	-0.60	1.02	-0.11	2.58	17.33
1.83	1.10	1.02	0.11	2.50	13.82

Table A.1: Average y-velocity in 10 planes of RMCA multiplied with the amount of pixels per slice to simulate mass flow (Fig. 4.2).

$t = 0.000$ s		$t = 0.658$ s		$t = 0.940$ s	
Flow (ml/s)	Deviation from median (%)	Flow (ml/s)	Deviation from median (%)	Flow (ml/s)	Deviation from median (%)
0.92	14.04	0.47	14.04	1.45	14.04
0.88	8.77	0.45	8.77	1.38	8.77
0.84	3.51	0.43	3.51	1.32	3.51
0.81	0.00	0.41	0.00	1.27	0.00
0.77	-5.26	0.39	-5.26	1.20	-5.26
0.75	-7.02	0.38	-7.02	1.18	-7.02
0.79	-1.75	0.41	-1.75	1.25	-1.75

Table A.2: Average z-velocity in 7 planes of BA multiplied with the amount of pixels per slice to simulate mass flow.

$t = 0.000$ s		$t = 0.658$ s		$t = 0.940$ s	
Flow (ml/s)	Deviation from median (%)	Flow (ml/s)	Deviation from median (%)	Flow (ml/s)	Deviation from median (%)
0.38	-29.61	0.26	-34.52	0.41	62.18
0.52	-3.90	0.34	-14.14	0.15	-39.60
0.50	-7.43	0.39	-0.35	0.28	10.79
0.56	2.52	0.38	-3.79	0.10	-60.07
0.48	-12.10	0.39	0.00	0.01	-97.43
0.54	0.00	0.43	8.56	0.25	0.00
0.63	15.32	0.44	12.10	0.23	-6.98
0.59	8.20	0.40	0.70	0.34	36.39
0.61	12.78	0.39	0.03	0.42	66.88

Table A.3: Average x-velocity in 9 planes of RPCoA multiplied with the amount of pixels per slice to simulate mass flow.

A.2. Mesh Sensitivity studies

A.2.1. Aneuysm reduced geometry

A mesh sensitivity study has been done for the CFD challenge aneurysm. In Table A.4 the specifics of this study can be found.

Mesh	Amount of cells	Average WSSTA value
Coarse	800.000	3.2908 Pa
Fine	2.250.000	3.3114 Pa

Table A.4: Mesh sensitivity study, the difference between the two values is 0.6 %.

A.2.2. CFD challenge

A mesh sensitivity study has been done for the CFD challenge aneurysm. In Table A.5 the specifics of this study can be found.

Mesh	Amount of cells	Average WSSTA value
Coarse	600.000	3.8691 Pa
Fine	1.800.000	3.8743 Pa

Table A.5: Mesh sensitivity study, the difference between the two values is 0.1 %.

A.3. AMC aneurysm results

The WSSTA and OSI values are shown in Figure A.1. The WSSTA value is scaled to a maximum value of 1 Pa, so that the locations with a low WSS value are visible.

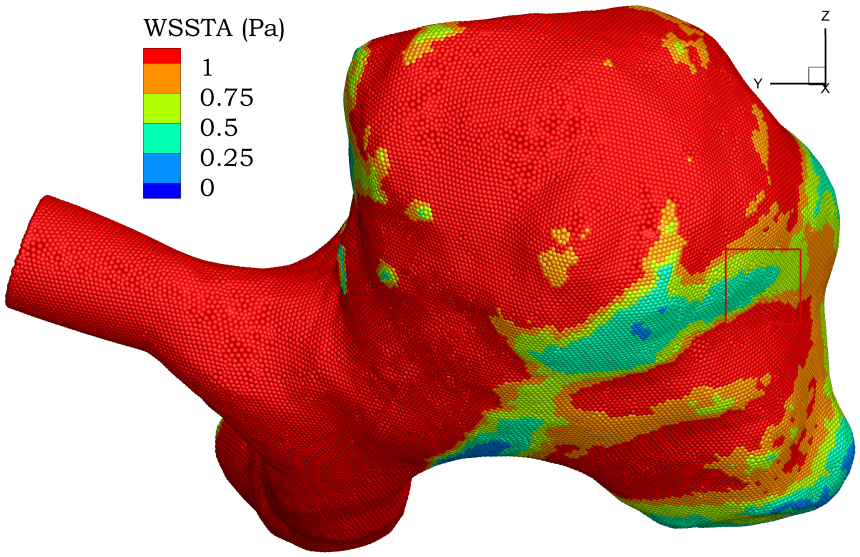

(a) WSSTA aneurysm

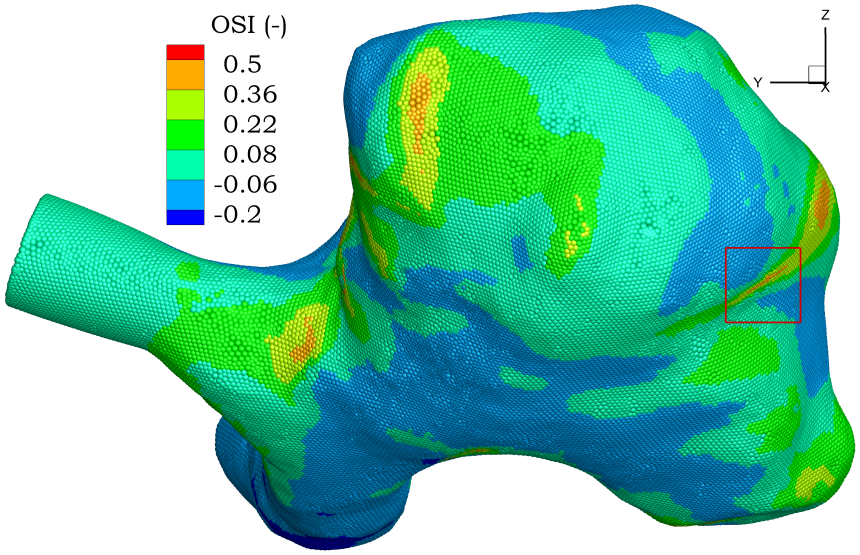

(b) OSI aneurysm

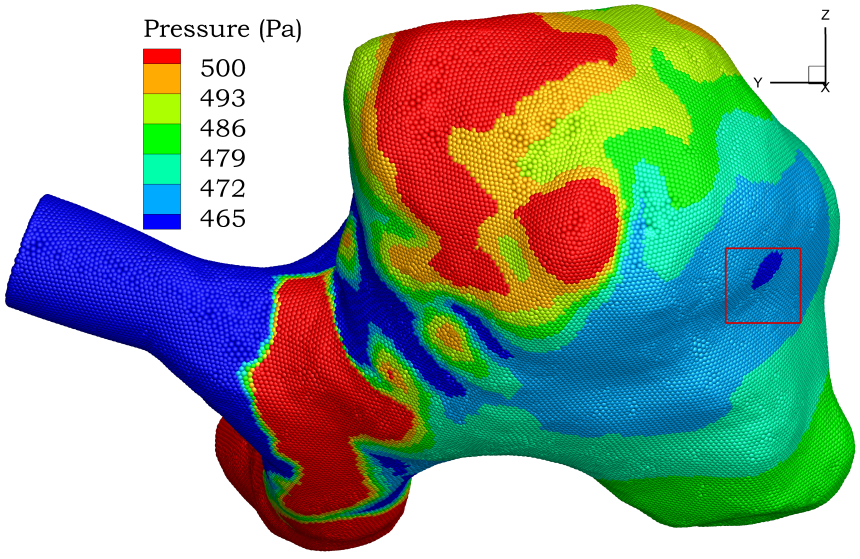

(c) Pressure aneurysm

Figure A.1: WSSTA, OSI and pressure values for the aneurysm model

B

Matlab routines

B.1. MRI data visualization

```
%% Matlab script to visualize MRI data
% This script reads the 5D velocity vector (x, y, z, u, t)
% and plots the slices in the z-direction.
outputData = load('velocity.mat');

clear D
clear Dn
for i=1:3
    D(:,:,i,:) = outputData.velocity(120:210,140:240,3:39,i,11);
end

Dn(:,:,1,:) = flip(sqrt(D(:,:,1,:).^2 +...
    D(:,:,2,:).^2 +D(:,:,3,:).^2),2);

Dxyzv(:,:,:) = Dn(:,:,1,:);
Dxyzv(Dxyzv == 0) = NaN;
dim = size(Dxyzv);
x = 1:dim(1)';
y = 1:dim(2);
[x,y] = meshgrid(1:dim(1),1:dim(2));
z = double(isfinite(Dxyzv));
z(z == 0) = NaN;
hold all
for i = 1:4:dim(3)
    h = surf(x',y',i*z(:,:,i),Dxyzv(:,:,i), 'FaceColor','interp');
    set(h, 'edgecolor','none')
    colormap('jet')
end
```

B.2. Rupture risk calculations

```
%% Rupture risk calculation for an aneurysm
```

```
%specify which one
filename_prefix = 'challengeparab';
viewAn = [75 0];%255, 75
load(filename_prefix);

%% Isolate aneurysm
indexxy = intersect(find(A.data(:,3)<0.0106),find(A.data(:,4)<0.014));
percentage = 0.1;


%% Criteria
indexOSI = find(OSI > (1-percentage)*(max(OSI(indexxy))-min(OSI(indexxy)))...
    +min(OSI(indexxy)));
indexWSSTA = find(WSSmagav < percentage*(max(WSSmagav(indexxy))-...
min(WSSmagav(indexxy)))+min(WSSmagav(indexxy)));
indexPressure = find(pressure(:,58) < percentage*(max(pressure(indexxy,58))-...
    min(pressure(indexxy,58)))+min(pressure(indexxy,58)));


riskmatrix = zeros(length(OSI),1);
riskmatrix(indexOW) = riskmatrix(indexOW) + 2;
riskmatrix(indexOWP) = riskmatrix(indexOWP) + 1;
csvwrite('challengeparab.txt',[A.data(:,2) A.data(:,3) A.data(:,4) ...
    riskmatrix OSI WSSmagav pressure(:,58)])
```

C

VMTK code

The code used for the smoothing and preparation of the geometry can be found below.

```
vmtksurfacereader -ifile H:/filename.stl --pipe vmtksurfacewriter
    -ofile H:/filename.vtp
vmtksurfaceviewer -ifile H:/filename.vtp
vmtksurfacesmoothing -ifile H:/filename.vtp -passband 0.45 -iterations
    100 -boundarysmoothing 0 --pipe vmtksurfacesubdivision -method
    triangle -ofile H:/filename_s.vtp
vmtksurfaceviewer -ifile H:/filename_s.vtp
vmtksurfaceclipper -ifile H:/filename_s.vtp -ofile
    H:/filename_sc.vtp
vmtksurfacereader -ifile H:/filename_sc.vtp --pipe vmtkcenterlines
    -seedselector openprofiles --pipe vmtksurfacewriter -ofile
    H:/filename_scc.vtp
vmtksurfacereader -ifile H:/filename_scc.vtp --pipe
    vmtkflowextensions -adaptivelength 0 -extensionmode boundarynormal
    -interactive 0 -boundarypoints 50 -transitionratio 0.8 -sigma 0.1
    -extensionlength 3 -extensionratio 10 --pipe vmtksurfacecapper
    -method centerpoint -interactive 0 --pipe vmtksurfacewriter
    -ofile H:/filename_scce.vtp
vmtksurfaceviewer -ifile H:/filename_scce.vtp
vmtksurfacereader -ifile H:/filename_scce.vtp --pipe vmtksurfacewriter
    -ofile H:/filename_scce.stl
```

D

Running simulations on the cluster

The transition of producing results from simulations in a GUI on a computer to producing them on the cluster is a process that is not too straight forward. This Chapter will function as a step-by-step guide of this transition.

First, assuming that a working simulation has run on the computer, a case file (`.cas.gz`) has to be saved. This is the file that will be sent to the cluster to perform the simulation from. In this case file the main settings will remain the same, but a few have to be redefined in a journal file (`.jou`).

The journal file uses the same commands as the Text User Interface (TUI) does in Fluent. This mode can be activated by typing 'Enter' in the text screen on the bottom right. In the journal file, all dialog prompts are written down and separated by spaces. Before uploading a journal file, always make sure that the file works on your own computer, by either reading the file as a whole from the File>Read...>Journal menu, or by copying the lines in the TUI.

The journal file starts with the command to start a transcript and a line to enable Fluent to run in batch mode:

```
/file/start-transcript "cyviscosityon.trn" ok
/file/set-batch-options , yes ,
```

After these lines, the case file is loaded, together with the UDFs that have to be interpreted.

```
/file/read-case/ "filename.cas.gz" ok
/define/user-defined/interpreted-functions "UDF.c" "cpp" 10000 no
```

All settings affected by the UDF have to be defined in the journal file. This means that for every boundary the UDF boundary conditions have to be set, as well as for the initial conditions. In this study, this looks like this:

```
/define/boundary-conditions/pressure-outlet outlet_rsca yes no 0 no
    yes no no yes yes yes "udf" "TargMassFlowOut" no 5000000 no 1
/define/boundary-conditions/pressure-outlet outlet_lsca yes no 0 no
```

```
    yes no no yes yes yes "udf" "TargMassFlowOut" no 5000000 no 1
/define/boundary-conditions/pressure-outlet outlet_raca yes no 0 no
    yes no no yes yes yes "udf" "TargMassFlowOut" no 5000000 no 1
/define/boundary-conditions/pressure-outlet outlet_laca yes no 0 no
    yes no no yes yes yes "udf" "TargMassFlowOut" no 5000000 no 1
/define/boundary-conditions/pressure-outlet outlet_rmca yes no 0 no
    yes no no yes yes yes "udf" "TargMassFlowOut" no 5000000 no 1
/define/boundary-conditions/pressure-outlet outlet_lmca yes no 0 no
    yes no no yes yes yes "udf" "TargMassFlowOut" no 5000000 no 1
/define/boundary-conditions/pressure-outlet outlet_rpca yes no 0 no
    yes no no yes yes yes "udf" "TargMassFlowOut" no 5000000 no 1
/define/boundary-conditions/pressure-outlet outlet_lpca yes no 0 no
    yes no no yes yes yes "udf" "TargMassFlowOut" no 5000000 no 1
/define/boundary-conditions/velocity-inlet inlet_ba no no yes yes
    yes yes "udf" "ParabProfileTrans_BA" no 0
/define/boundary-conditions/velocity-inlet inlet_lica no no yes yes
    yes yes "udf" "ParabProfileTrans_LICA" no 0
/define/boundary-conditions/velocity-inlet inlet_rica no no yes yes
    yes yes "udf" "ParabProfileTrans_RICA" no 0
/define/materials/change-create blood blood no no no yes user-defined
    "cy_viscosity" no no no
```

When the UDFs are loaded, the solution has to be initialized, in this case with a hybrid initialization. Next to that, the frequency and contents of the automatically saved data file are prescribed. When a data file (`.dat/.dat.gz`) is available from former time steps or simulations, the line with the hybrid initialization can be put in comment mode by putting a ; in front. When a data file is loaded, all transient simulations will start from the time step provided in this data file.

```
;/solve/initialize/hyb-initialization ok
/file/read-data/ "filename-timestep.dat.gz"
/file/auto-save/data-frequency 10
/file/data-file-options y x-velocity y-velocity z-velocity
    velocity-magnitude x-wall-shear y-wall-shear z-wall-shear
    wall-shear x-vorticity y-vorticity z-vorticity vorticity-mag
    strain-rate-mag pressure dynamic-pressure absolute-pressure
```

At last, the size of the time step, the number of iterations per time step and the number of time steps have to be set, as well as the command to save the case file when the simulation is finished. Then the procedure can be finished with the `exit` command.

```
/solve/set/time-step 0.001
/solve/dual-time-iterate 290 100
wcd cyviscosityon.cas.gz ok
exit ok
```

The journal file is called by the bash file (`.sh`), which provides more top-level information to the cluster. This file contains the number of cores and nodes that have to be used for the simulation, the version of Fluent, etc.

More information on writing journal files and the TUI can be find on several (CFD) fora online, this guide should help to get up to speed, but more specific information can best be searched

for when needed.